Single-mRNA imaging and modeling reveal coupled translation initiation and elongation rates

Irene Lamberti[1], **Jeffrey A. Chao**[2], **Cédric Gobet**[1*], **Felix Naef**[1*]

***For correspondence:**
felix.naef@epfl.ch (FN);
cedric.gobet@epfl.ch (CG)

[1]Laboratory of Computational and Systems Biology, Institute of Bioengineering, Faculty of Life Sciences, École Polytechnique Fédérale de Lausanne (EPFL), Lausanne, Switzerland; [2]Friedrich Miescher Institute for Biomedical Research, 4056 Basel, Switzerland

Abstract mRNA translation involves multiple regulatory steps, but how translation elongation influences protein output remains unclear. Using SunTag live-cell imaging and mathematical modeling, we quantified translation dynamics in single mRNAs across diverse coding sequences. Our Totally Asymmetric Exclusion Process (TASEP)-based Hidden Markov Model (HMM) revealed a strong coordination between initiation and elongation rates, resulting in consistently low ribosome density (≤12% occupancy) across all reporters. This coupling persisted under pharmacological inhibition of the elongation factor eIF5A, where proportional decreases in both initiation and elongation rates maintained homeostatic ribosome density. In contrast, eIF5A knockout cells exhibited a significant decrease in ribosome density, suggesting altered coordination. Together, these results highlight a dynamical coupling of initiation and elongation rates at the single-mRNA level, preventing ribosome crowding and maintaining translational homeostasis in mammalian cells.

Introduction

Regulation of protein synthesis is essential for cellular homeostasis and adaptive responses to external stimuli. While the untranslated regions (UTRs) of messenger RNA (mRNA) have traditionally been recognized for their central role in translation initiation (***Hinnebusch et al., 2016***; ***Mayr, 2018***), the influence of the coding sequence (CDS) on initiation remains unclear. Indeed, in a simple model where elongation is much faster than initiation, heterogeneity in elongation rates has no impact on the total protein output per mRNA (***Plotkin and Kudla, 2011***; ***Shah et al., 2013***; ***Erdmann-Pham et al., 2020***). This view is supported by measurements indicating that initiation happens a few times per minute, while elongation proceeds at 2–6 aa/s (***Boersma et al., 2019***; ***Yan et al., 2016***; ***Mateju et al., 2020***; ***Livingston et al., 2023***; ***Madern et al., 2025***), suggesting that initiation is the rate-limiting step in mammalian translation.

However, this paradigm is being challenged by recent findings highlighting the CDS itself as a critical regulator of translational dynamics. In particular, specific CDS features can affect ribosome elongation, triggering surveillance pathways that sense ribosome stalling and collisions (***Juszkiewicz et al., 2020***; ***Li et al., 2022***; ***Barrington et al., 2023***; ***Bicknell et al., 2024***; ***Madern et al., 2025***). Some of these pathways, such as ribosome quality control (RQC), can induce ribosome recycling and mRNA degradation (***Wu et al., 2020***; ***Goldman et al., 2021***; ***Buschauer et al., 2020***), whereas others down-regulate translation initiation in *cis* by recruiting regulatory complexes to stalled ribosomes (***Amaya Ramirez et al., 2018***; ***Hickey et al., 2020***; ***Juszkiewicz et al., 2020***). This

suggests that cells have the capacity to monitor elongation rates and ribosome density at the level of individual mRNAs, responding by adjusting initiation or degrading aberrant transcripts (***Joazeiro, 2019***). Nevertheless, a comprehensive quantitative understanding of how elongation rates feedback on initiation in mammalian systems, at both bulk and single-mRNA levels, is still lacking. Furthermore, it is still unclear whether this coupling mechanism allows cells to dynamically adapt translation in response to environmental or physiological stress, such as nutrient deprivation, oxidative stress, or inhibition of specific translation factors. Clarifying this would shed light on the broader role of initiation–elongation feedback in translational homeostasis.

Elongation rates along transcripts depend on several factors including aminoacyl-tRNA availability, codon-anticodon interactions, co-translational folding, and biochemical properties of certain amino acids (***Neelagandan et al., 2020***; ***Madern et al., 2025***). Notably, peptide-bond formation is particularly slow with multiple proline (P) residues, as proline is both a weak donor and acceptor in peptidyl transfer (***Lassak et al., 2015***). With poly-proline motifs being abundant in mammals, cells have evolved eukaryotic initiation factor 5A (eIF5A), bearing a unique hypusination modification, to facilitate peptide-bond formation. Although initially thought to act primarily at poly-proline motifs (***Gutierrez et al., 2013***; ***Lassak et al., 2015***; ***Huter et al., 2017***), later studies have suggested a broader role for hypusinated eIF5A (h-eIF5A) in translation elongation (***Schuller et al., 2017***; ***Pelechano and Alepuz, 2017***; ***Manjunath et al., 2019***). eIF5A therefore represents a key factor in modulating context-dependent translation elongation, making it a prime target for exploring the interplay between coding sequence, elongation, and initiation.

A conceptual framework commonly used to model translation is the Totally Asymmetric Exclusion Process (TASEP), where ribosomes are treated as particles stochastically hopping along the mRNA (modeled as a 1D lattice) (***Zia et al., 2011***; ***Sharma et al., 2019***; ***Szavits-Nossan and Ciandrini, 2019***; ***Erdmann-Pham et al., 2020***). In this framework, entry and exit rates correspond to initiation and termination, respectively, while the hopping rate represents elongation. Under conditions where initiation is rate-limiting, TASEP predicts a “low-density” regime featuring sparse ribosome loading and minimal collisions (***Riba et al., 2019***).

While the TASEP provides a strong theoretical basis for understanding translation, extending it to capture single-mRNA heterogeneity and dynamic fluctuations in initiation and elongation is a persistent challenge (***Zia et al., 2011***; ***Szavits-Nossan et al., 2018***; ***Andreev et al., 2018***; ***Levin and Tuller, 2018***). Advances in single-molecule imaging, particularly the SunTag system, enable real-time monitoring of multiple rounds of translation on individual mRNAs (***Tanenbaum et al., 2014***; ***Yan et al., 2016***). However, most analyses of SunTag data rely on averaging signals across many transcripts, thereby masking transcript-to-transcript variability (***Morisaki and Stasevich, 2018***; ***Aguilera et al., 2019***). While a model that assigns distinct initiation and elongation rates to each transcript would offer deeper insights, this is complicated by the fact that the fluorescence of one translation site is the sum of the signals of multiple translating ribosomes. Because the fluorescence intensity is constant after the SunTag and the noise is usually large, inferring the position of single ribosomes on the mRNA is extremely challenging.

In this study, we develop a framework that decodes individual single-mRNA traces while simultaneously estimating global initiation and elongation parameters, allowing us to leverage single-molecule resolution without requiring explicit knowledge of ribosome positions on each transcript. We applied our model to investigate how CDS features modulate translation elongation and initiation in mammalian cells, using single-molecule (SunTag) imaging in HeLa cells (***Weidenfeld et al., 2009***; ***Voigt et al., 2017***; ***Tanenbaum et al., 2014***). Specifically, we designed multiple SunTag reporters differing only in codon content in the second half of the CDS, comparing proline-rich sequences such as those of collagen type I alpha 1 (COL1A1), highly dependent on h-eIF5A (***Barba-Aliaga et al., 2021***), to minimal or alanine-rich inserts. We acquired SunTag traces with and without harringtonine treatment. Our TASEP-based model allowed us to infer reporter-specific translation kinetics and ribosome number over time for each trace. We further exploit the role of eIF5A by perturbing elongation via pharmacological inhibition and genetic knockout, thereby examining the

effects on ribosome density and initiation. Overall, our study contributes new tools for analyzing SunTag data and provides broader insights into how translational parameters are dynamically regulated to maintain protein synthesis homeostasis.

Results

Translation exhibits bursts with low average ribosome density

To image translation of single mRNAs over time in living cells, we used the SunTag system (***Tanenbaum et al., 2014***), which fluorescently tags nascent protein chains on individual transcripts. The SunTag encodes an array of 24 GCN4 epitopes recognized by single-chain variable fragment antibodies fused to a super-folder GFP (scFv-GFP). When this tag is placed upstream of a sequence of interest, newly synthesized peptides emerging from the ribosome exit tunnel are rapidly bound by scFv-GFP (***Yan et al., 2016***). The mRNA itself is fluorescently labeled with an MS2-MCP system (***Figure 1***A).

To investigate the influence of coding sequence on translation elongation and initiation, we derived multiple reporters from the SunTag-Renilla-MS2 system (***Voigt et al., 2017***), substituting the Renilla sequence with different inserts (***Figure 1***A, B). We designed a proline-rich reporter (PPG) containing a COL1A1 subsequence rich in proline-proline-glycine (P/P/G) repeats, which are known to induce ribosome stalling and depend on eIF5A activity (***Barba-Aliaga et al., 2021***; ***Gutierrez et al., 2013***; ***Schuller et al., 2017***; ***Pelechano and Alepuz, 2017***). As controls, we generated two additional reporters: one in which the proline codons in the COL1A1 subsequence were replaced with alanine (AAG), a neutral amino acid encoded by fast-translating codons (***Gobet et al., 2020***), to minimize stalling and possible eIF5A dependence; and another with no insert sequence (no-insert) as a control for SunTag protein synthesis. The original SunTag-Renilla-MS2 reporter (Renilla) was also included in our analysis (***Figure 1***B). Together, these four constructs allowed us to systematically compare the translation dynamics of mRNAs with varying coding sequences and to evaluate the impact of elongation perturbation on translation kinetics.

All reporters were stably integrated into HeLa cells under a doxycycline-inducible promoter (***Weidenfeld et al., 2009***). The cell line also stably expresses scFv-GFP antibodies against the SunTag together with NLS-stdMCP-stdHalo-RH1 recognizing the MS2 loop (MCP) while binding to the actin cortex (RH1), stabilizing the mRNA for long-term imaging (***Bhaskar et al., 2020***) (***Figure 1***C).

Using a spinning-disk confocal microscope, we imaged translation over several minutes (***Figure 1—figure Supplement 1***A and ***Figure 1—video 1***), observing a highly dynamic and heterogeneous process characterized by active and inactive periods (***Figure 1***D). We quantified the duration of these periods empirically, by measuring the duration of silent (inactive) and translated (active) periods. In most experiments, more than 50% of mRNAs were translated (***Figure 1***E) with a mean trace duration exceeding 10 minutes (***Figure 1—figure Supplement 1***B). We quantified the duration of translated and silent periods (***Figure 1***F), finding that active translation typically lasts around 10–15 minutes, interspersed with shorter silent periods of approximately 5–10 minutes across all reporters (***Figure 1***G). The slightly shorter translated periods observed for the no-insert reporter are likely due to its shorter length, which allows observation of isolated bursts more frequently.

We established an experimental method to measure the intensity of one mature protein, allowing us to estimate the number of translating ribosomes across translated periods. The measurement of mature proteins is challenging due to their rapid diffusion and low intensity against the high background of unbound scFv-sfGFPs. To overcome this, we used a SunTag-Renilla-RH1 construct to tether mature proteins to the actin cytoskeleton (***Voigt et al., 2017***). However, as these spots remained too dim at experimental laser powers, we developed an intensity-power calibration assay. This allowed us to measure spot intensity at high power and extrapolate the value for live-imaging conditions (14 ± 2 a.u., Methods and ***Figure 1—figure Supplement 2***A–C). No-insert, AAG and Renilla reporters showed on average less than 10 ribosomes per mRNA (***Figure 1—figure Supplement 2***D), while the PPG reporter showed a slightly higher number (12 ribosomes per mRNA).

Assuming a uniform ribosome distribution along the transcript during a translated period, these observations imply a low ribosome density, with 7-12% of the transcript length covered by ribosomes, on average (***Figure 1***H). However, given the observed bursting dynamics, the actual ribosome distribution may deviate from a uniform distribution, potentially resulting in higher local ribosome densities. Nevertheless, our data show that, independently of the reporter sequence, bursting dynamics and ribosome densities were very similar, although this does not inform on the relative contributions of initiation and elongation to these observations. Finally, the observation of bursting behavior is in agreement with what was measured ***Livingston et al.*** (***2023***) for other SunTag reporters.

TASEP-based inference of translation dynamics from single run-off traces

To gain more information on the translation dynamics, we performed harringtonine (HT) run-off assays, under the same imaging conditions (***Figure 2—figure Supplement 1***A, ***Figure 2—video 1*** and ***Figure 2—video 2***). HT blocks the first step of elongation after subunit joining, while allowing translating ribosomes to elongate and terminate (***Fresno et al., 1977***). The time required for the SunTag signal to disappear approximates the total elongation time, but depends on the position of the last (most upstream) elongating ribosome when HT blocks initiation. Because the distribution of ribosomes on each transcript is unknown, it is common practice to average the signal from multiple traces to estimate the total elongation time (hence, the average ribosome speed) (***Yan et al., 2016***; ***Wang et al., 2016***; ***Mateju et al., 2020***; ***Aguilera et al., 2019***). Although this pseudo-bulk approach has been successful to estimate average elongation times, it has the limitation of neglecting trace-to-trace heterogeneity.

Here we used a novel approach, allowing us to infer the number of translating ribosomes over time at the single-mRNA level. In particular, we used a Hidden Markov Model (HMM), where the hidden states represent the number of ribosomes translating the SunTag reporter during the run-off (***Figure 2***A and Methods). The transition probabilities between hidden states were derived from an approximation of the Totally Asymmetric Exclusion Process (TASEP), assuming low ribosome density and homogeneous elongation rates. These probabilities define the likelihood of observing one or more termination events per imaging time step. This approach allowed us to relate the observed run-off times to the underlying initiation (α) and elongation rates (λ) (***Figure 2***A), as well as to decode single traces by inferring the number of translating ribosomes over time (***Figure 2***B). We assumed that HT takes 60 seconds to diffuse into the cells and effectively block initiation (***Ingolia et al., 2009***; ***Aguilera et al., 2019***).

In our model, we accounted for the finite size of the SunTag by calculating correction factors for the intensity mean and variance ($\gamma(t)$ and $\nu(t)$, Methods). In particular, $\gamma(t)$ generalizes the time-independent correction factor previously derived by others (***Aguilera et al., 2019***) to the run-off dynamics (***Figure 2***C and Methods). We first tested these approximations by comparing them with numerical simulations of the homogeneous ℓ-TASEP (Methods). We used different initiation and elongation rates, corresponding to a broad range of ribosome densities. These simulations confirmed the validity of our analytical approximations at low ribosome densities (***Figure 2***C, D and ***Figure 2—figure Supplement 2***A).

We then tested the performance of the model on simulated SunTag traces, with different values of the kinetic parameters and ribosome density ($\rho = 0.01 - 0.5$, i.e. average fraction of occupied transcript) (***Figure 2***E). Instead of fixing the mature protein intensity i_{MP}, we used the model to infer its value, alongside α and λ. This parameter determines the extent of the intensity drop due to a termination event. The kinetic parameters and the mature protein intensity are accurately inferred at low density ($\rho \lesssim 10\%$) for different noise levels (***Figure 2***E), despite some correlation between α and i_{MP} (***Figure 2—figure Supplement 2***B). The correlation is more pronounced at higher density, where i_{MP} is underestimated and α is overestimated. Importantly, the average ribosome density is overestimated at high densities – we are neglecting ribosome interference that can reduce the effective initiation rate – while it is accurately inferred at low densities (***Figure 2—figure***

Supplement 2C).

Low ribosome density arises from coordinated translation initiation and elongation

After testing our model on simulated traces, we used it to analyze the HT run-off assays. To avoid correlations between parameters, we fixed the value of i_{MP} to the experimentally measured value (14 ± 2 a.u.). We modeled intensity noise as lognormal and estimated its magnitude from cycloheximide-treated traces (Methods and ***Figure 3—figure Supplement 1***). The model allowed us to estimate the number of ribosomes translating the mRNA for each translation site, and thus the total run-off time for each trace (i.e., the time at which the number of translating ribosomes reaches zero) (***Figure 3***A, violin plot). These single-trace estimates revealed substantial variability in run-off times, which likely reflects elongation heterogeneity and stalling events beyond what can be explained by differences in initial ribosome distribution.

However, for some traces, the mRNA signal was lost before run-off completion (***Figure 3***A, histogram). This occurred rarely for the no-insert reporter, while for the Renilla and PPG reporters, we observed about 10-20% of incomplete traces. Surprisingly, the AAG reporter showed up to 50% of incomplete traces per experiment and longer run-off times, suggesting considerable ribosome stalling (***Figure 3***A). The elongation rates inferred by our model for the no-insert, PPG and Renilla reporters ranged from 2 to 4.5 aa/s, consistent with previous reports (2–6 aa/s) (***Yan et al., 2016***; ***Mateju et al., 2020***; ***Livingston et al., 2023***; ***Madern et al., 2025***) (***Figure 3***B). As we expected from the run-off times distribution, the AAG reporter was markedly slower, with elongation rates close to 1 aa/s (***Figure 3***B).

It is common practice (***Yan et al., 2016***; ***Wang et al., 2016***; ***Mateju et al., 2020***; ***Aguilera et al., 2019***) to infer the total elongation time by fitting a linear decay to the average run-off intensity, usually discarding the slower decay resulting from heterogeneity in elongation (***Wang et al., 2016***). The intercept between the fast linear decay and the x-axis gives an estimate of the total average elongation time (***Figure 3—figure Supplement 2***A). Our single-trace inference method tends to estimate lower elongation speeds with respect to what was obtained with the population-averaged linear fit (***Figure 3—figure Supplement 2***A–B). This is likely because our model accounts for the initial ribosome distribution and is more sensitive to trace-to-trace translation heterogeneity. In addition, the HMM allowed us to decode the single-mRNA traces and estimate the time between consecutive termination events, which significantly deviated from an exponential distribution (***Figure 3—figure Supplement 2***C). This can be partially explained by bursting; however, since initiation is inhibited upon HT treatment, waiting times between termination events that are much longer than the average elongation time most likely reflect persistent ribosome stalling.

The inferred initiation rates corresponded to ∼1-2 ribosomes per minute (***Figure 3***C), close to what was measured in similar systems (1 – 5 ribosomes per min) (***Boersma et al., 2019***; ***Barrington et al., 2023***). Surprisingly, the AAG reporter showed markedly lower initiation rates (***Figure 3***C). From the elongation and initiation rates, we calculated the average ribosome density under the low-density assumption (***Figure 3***D, Methods ***Equation 14***). Despite the variability in elongation rates, we obtained low densities for all reporters, remarkably similar to our previous estimates (***Figure 1***H). Furthermore, we observed a significant correlation between initiation and elongation rates (Pearson correlation coefficient $r = 0.85$, average density $\rho = 0.08$) (***Figure 3***E). This suggests a tight feedback between initiation and elongation, where changes in one rate are compensated by changes in the other to maintain a low ribosome density.

eIF5A perturbations minimally affect ribosome density and translational bursting

Having established a correlation between initiation and elongation rates across reporters, we next aimed to investigate the impact of perturbing translation elongation on initiation and ribosome density. We chose to target eIF5A, a protein known to play a crucial role in ribosome elongation (***Schuller et al., 2017***; ***Pelechano and Alepuz, 2017***; ***Manjunath et al., 2019***). eIF5A activity was

modulated using two distinct approaches. First, HeLa cells were incubated for 24 hours with 1 μM and 10 μM GC7. GC7 is a spermidine analog that inhibits Deoxyhypusine synthase (DHPS), the enzyme responsible for hypusination of eIF5A, thereby reducing the levels of active, hypusinated eIF5A (h-eIF5A) (***Barba-Aliaga et al., 2021***; ***Giraud et al., 2020***; ***Schultz et al., 2018***; ***Coni et al., 2020***; ***Szepesi et al., 2023***; ***Matsumoto et al., 2023***). Upon treatment, h-eIF5A levels were reduced by ~ 2- and ~ 3-fold, respectively, while total eIF5A levels remained unchanged (***Figure 4***A). To minimize potential side effects of GC7, we selected the 1 μM concentration throughout our experiments. As a second approach, we generated a CRISPR/Cas9 eIF5A knockout (KO) cell line derived from the PPG-expressing HeLa cells. This KO cell line exhibited a complete loss of both total and hypusinated eIF5A (***Figure 4***B).

Upon doxycycline (DOX) induction, both GC7-treated cells and eIF5A KO cells showed expression of the SunTag reporters and exhibited active translation (***Figure 4***C–E, ***Figure 4—figure Supplement 1***A, ***Figure 4—video 1*** and ***Figure 4—video 2***), with no significant difference in the fraction of translated mRNA (***Figure 4***F) and translated trace duration (***Figure 4—figure Supplement 1***B). As for control conditions, the translation signal showed bursting dynamics (***Figure 4***E), with duration of translated and untranslated periods similar to the control (***Figure 4***G, H). Ribosome density was remarkably stable between control and perturbed conditions, with no statistically significant differences (***Figure 4***I). In summary, these findings indicate that decreasing eIF5A activity or level has a minimal effect on translational bursting and ribosome density in our system.

eIF5A-driven elongation changes induce initiation regulation to preserve ribosome density

To understand how elongation and initiation contribute to maintaining low ribosome density upon eIF5A perturbations, we performed HT run-off experiments on GC7-treated and eIF5A KO cells, alongside control conditions (***Figure 5***A, ***Figure 5—figure Supplement 1***A, ***Figure 5—video 1***, ***Figure 5—video 2*** and ***Figure 5—video 3***).

Using our TASEP-based model, we evaluated the intensity of a single mature protein by jointly fitting control and perturbed conditions with a shared i_{MP} parameter, while still allowing condition-specific initiation and elongation rates (***Figure 5—figure Supplement 2***A). Strikingly, the inferred i_{MP} values closely matched the independently measured intensity of (14 ± 2) a.u. (***Figure 5—figure Supplement 2***B). This close quantitative agreement, combined with the absence of any significant correlation between α and i_{MP} (***Figure 5—figure Supplement 2***C), indicates that the model recovers this parameter robustly rather than compensating for other rates. Given this strong internal consistency between measurement and inference, we fixed i_{MP} to its experimentally determined value for all subsequent analyses.

After 24 hours of GC7 treatment, we observed an increase in the average run-off time across all reporters (***Figure 5***A). The subset of traces showing slow run-off (≥15 min) – $< 4\%$ in control conditions, with the exception of the AAG – increased significantly upon GC7 treatment (11% for no-insert, 18% for PPG and 40% for Renilla) (***Figure 5***B). The average total elongation time inferred with our model also increased for all reporters (***Figure 5***C). The extent of the increase varied across experiments for no-insert and Renilla: 2 and 8-fold changes for no-insert and 8 and 5-fold changes for Renilla. More consistent although milder increases were observed for PPG, both upon GC7 treatment (2-fold change) and eIF5A KO (1.5-fold). The already slow AAG reporter was only mildly affected (1.4-fold change). Our HMM inference results confirmed a general decrease in elongation rates in both GC7-treated and eIF5A KO cells (***Figure 5***D). Importantly, we also observed a concurrent decrease in initiation rates under both perturbation conditions (***Figure 5***E).

In GC7-treated cells, both elongation and initiation rates decreased proportionally (***Figure 5***D,E), resulting in a nearly constant ribosome density (***Figure 5***F, G). This is consistent with our previous observations (***Figure 4***I), which showed that average ribosome density was largely unaffected by the GC7 treatment. However, the eIF5A KO cells revealed a different outcome. While elongation rates also decreased in the KO, the magnitude of the decrease was less pronounced compared to

GC7 treatment (***Figure 5***D). In particular, the fraction of traces showing a slow run-off (***Figure 5***A, right tail, and ***Figure 5***B) was reduced in eIF5A KO with respect to GC7 treatment (18% in GC7 treatment and 9% in eIF5A KO). At the same time, initiation was strongly decreased (***Figure 5***E). As a result, we observed a significant reduction in average ribosome density in the eIF5A KO cells (***Figure 5***F, G, 30–40% decrease), which we did not observe upon GC7 treatment. This can be explained by either faster elongation or more efficient stalling resolution via RQC mechanisms (***Latallo et al., 2023***; ***Goldman et al., 2021***). Overall, we observed that initiation is dynamically adjusted to elongation upon eIF5A perturbation, most likely to avoid ribosome crowding.

Discussion

By integrating single-mRNA imaging with single-trace statistical modeling, our study highlights key principles of translational regulation. First, we demonstrate that translation maintains remarkably low ribosome density ($\leq 12\%$ of the CDS occupied by ribosomes) across diverse coding sequences by coordinating initiation and elongation rates. Second, when elongation is perturbed by modulating eIF5A activity, initiation is proportionally adjusted to preserve low-density translation. Third, complete eIF5A knockout (KO) alters this coordination, suggesting differences in the sensing of ribosome stalling or collisions in the absence of eIF5A.

Our results support a model in which translation under homeostatic conditions occurs at low ribosome density, with initiation serving as the rate-limiting step (***Riba et al., 2019***; ***Boersma et al., 2019***; ***Livingston et al., 2023***). Indeed, using the SunTag system to visualize translation of single mRNAs, we consistently observed low density across all reporter mRNAs, regardless of coding sequence variations. This conserved feature may reflect an evolutionary strategy aimed at avoiding overuse of resources, as the same protein synthesis rate can be attained by engaging fewer ribosomes at the same time (***Erdmann-Pham et al., 2020***). Since the pool of free ribosomes may limit initiation (***Shah et al., 2013***), maximizing this pool may be beneficial for the cell, since it allows more rapid and flexible adaptation of initiation rates in response to changing demands. At the same time, by minimizing the frequency of transient, stochastic collisions that arise from high ribosome density, the cell enhances its ability to detect and respond to problematic translation events. Persistent ribosome collisions can serve as clear signals of aberrant translation and trigger mRNA degradation, in agreement with the observation that high ribosome occupancy can destabilize mRNAs (***Presnyak et al., 2015***; ***Bazzini et al., 2016***; ***Narula et al., 2019***; ***Wu et al., 2019***; ***Bae and Coller, 2022***; ***Bicknell et al., 2024***).

The low ribosome density across reporters stems from the dynamic interplay between elongation and initiation rates. Even though our mRNAs shared an identical 5' UTR, we observed significant and coupled variations in elongation and initiation across different coding sequences. It is important to note that this correlation is not a consequence of our model or inference, as the results on simulated data showed that we could infer a wide range of initiation and elongation rates, corresponding to very different densities. The strong correlation observed in real data suggests a feedback mechanism in which initiation is modulated by the prevailing elongation status, thereby preventing ribosome crowding and maintaining low density. The dynamic interplay between elongation and initiation has also recently been suggested in yeast (***Lyons et al., 2023***), in the case of mRNA reporters encoding synonymous codons. Similar conclusions have been reached in flies and humans for synonymous reporters, pointing to feedback mechanisms on translation initiation (***Barrington et al., 2023***). The main hypothesis underlying these observations in mammals is that suboptimal elongation leads to ribosome collisions, which are in turn sensed via molecular pathways that inhibit initiation.

The first response to ribosome collisions is the recruitment of the GIGYF2/4EHP complex, a cis-acting translational repressor that inhibits eIF4E binding and thus blocks further initiation (***Hickey et al., 2020***; ***Juszkiewicz et al., 2020***). The GIGYF2/4EHP complex can rapidly repress initiation upon the detection of collisions (whereas more persistent collisions initiate RQC, e.g. ZNF598-mediated degradation) (***Wu et al., 2020***). This molecular feedback on initiation, being transcript-specific,

could explain our observations, contrary to a more general response to collisions such as the Integrated Stress Response (ISR) and eIF2α phosphorylation, which would globally attenuate initiation (***Wu et al., 2020***). It is important to note that our reporters differ in codon content only far downstream of the translation start site (about 600 aa), which allows us to exclude the hypothesis of ribosomes queuing up to the initiation site and physically blocking initiation. Indeed, this would result in a high ribosome density, in contrast to our observations.

If collisions are long-lived, alternative molecular pathways, for example involving ZNF598, can induce RQC and, eventually, mRNA degradation. Also, beyond ribosome collisions, other mechanisms were shown to detect slow-elongating ribosomes in yeast, inducing ribosome recycling and mRNA degradation (***Buschauer et al., 2020***; ***Li et al., 2022***) – the evidence of similar pathways in mammals is still limited (***Absmeier et al., 2022***). Although our reporters showed a broad range of elongation rates (1-4 aa/s), there was no evidence of translation-dependent mRNA degradation, as we observed relatively consistent fractions of translated transcripts and trace duration distributions across reporters.

eIF5A plays a critical role in promoting elongation, especially in proline-rich sequences such as *COL1A1*. Thus, we next examined how perturbing eIF5A influences elongation, initiation, and ribosome density. Remarkably, significant reductions of active eIF5A – via GC7 treatment or genetic knockout – maintained largely consistent bursting dynamics and average ribosome densities compared to controls. However, run-off assays revealed different underlying mechanisms. GC7 treatment led to a coordinated decrease in both elongation and initiation rates, maintaining low ribosome density. Surprisingly, we observed stronger changes in run-off profiles for no-insert and Renilla compared to PPG, contrary to what was expected, as PPG contains known eIF5A-target motifs. It is possible that stronger stalling or collisions in PPG were masked by the RQC-mediated degradation of the SunTag reporter. Such degradation would lead to faster decay kinetics and could result in incorrect interpretation of the apparent translation dynamics (***Latallo et al., 2023***). Nevertheless, our perturbation experiment suggests that moderately impaired elongation due to reduced eIF5A activity triggers a feedback loop that dynamically adjusts initiation downwards, maintaining low-density translation.

eIF5A KO appeared to affect translation differently than GC7 treatment, leading to a significant (30–40%) reduction in ribosome density due to a stronger decrease in initiation than elongation. In particular, eIF5A KO showed fewer traces showing slow run-off compared to GC7, resulting in a milder decrease in elongation rate relative to control conditions. Although we do not have a definitive explanation for this observation, we hypothesize that the strong reduction in total eIF5A levels could alter the kinetics of stalling recognition and ribosome degradation. In yeast, eIF5A is known to compete with Not5 (CNOT3 in human (***Absmeier et al., 2022***)) for binding to the ribosomal E site (***Buschauer et al., 2020***). When peptidyl transfer is slow, eIF5A can occupy the E site and resolve stalling by promoting peptide-bond formation. Conversely, when decoding is slow, both the A and E sites remain unoccupied, allowing Not5 to bind the E site and mark the ribosome for degradation. Recently a similar mechanism was suggested in mammals (***Absmeier et al., 2022***). In this scenario, the absence of eIF5A could lead to more frequent or faster ribosome degradation, reducing the accumulation of stalled ribosomes and giving the appearance of a higher elongation rate. Ribosome recycling in normal conditions was recently estimated to take 22 min on average (***Madern et al., 2025***), but could be faster in the absence of eIF5A.

Interestingly, our attempt to optimize translation through proline-to-alanine substitutions in the COL1A1 PPG motif (AAG reporter) resulted in markedly slower elongation rates (~ 1 aa/s)) and increased frequency of incomplete run-off traces (50%). This suggests that expressing non-native sequences, even with seemingly favorable substitutions and a comparable codon adaptation index, can introduce unanticipated challenges, such as impaired RNA secondary structure or co-translational folding constraints. Specifically, replacing prolines with alanines reduced elongation by 60$\%$, likely due to disrupted co-translational folding. Given that prolines in collagen are critical for triple-helix formation (***Shoulders and Raines, 2009***), proline-to-alanine substitutions likely

generate misfolded intermediates that stall ribosomes (***Barba-Aliaga et al., 2021***; ***Komar et al., 2024***).

Limitations

First, our observations derive from exogenous mRNA, which may not fully recapitulate endogenous collagen translation dynamics, particularly given the absence of ER-coupled processing and secretory pathway targeting. This difference may explain the limited GC7 effects on the SunTag reporter, as recent studies suggest a direct role for eIF5A in ER-coupled collagen translation and translocation (***Rossi et al., 2013***; ***Mandal et al., 2016***; ***Barba-Aliaga et al., 2021***). This limitation could be partially overcome by genetically encoding the SunTag sequence via CRISPR/Cas9 genome editing, as performed by ***Dufourt et al.*** (***2021***) in Drosophila embryos. In addition, using an ER-specific SunTag reporter, as done in ***Choi et al.*** (***2025***) by adding a trans-membrane domain, would better recapitulate ER-coupled translation.

Second, while decoding individual traces, our model infers shared (population-level) rates. Inferring transcript-specific parameters would be more informative, but it is highly challenging due to the uncertainty regarding the initial ribosome distribution on single transcripts. Pooling multiple transcripts together allows some assumptions on the initial distribution that are essential for the inference of average elongation and initiation-rate parameters, while revealing substantial mRNA-to-mRNA variability in the posterior decoding (e.g., ***Figure 3—figure Supplement 2***C).

The deviation from an exponential distribution in the waiting times between termination events could arise from ribosome stalling, bursting, or a combination of both. Each of these effects would tend to bias our inference toward underestimating the true initiation rate. Incorporating explicit models of stalling and bursty initiation in future work would help make the inference framework more robust. In addition, our current model infers a single effective elongation rate per reporter, which averages ribosome dynamics across both the SunTag region and the variable CDS. As a consequence, it may underestimate true elongation-rate differences between the sequences of interest. This limitation could be alleviated by introducing distinct elongation parameters for the SunTag and the CDS, and by sharing the SunTag elongation parameter across different reporters. Incorporating all these features (stalling, bursting, SunTag-specific elongation rate) into the TASEP simulations would also make the simulated data more realistic.

Last, run-off assays are inherently variable and can underestimate or overestimate elongation rates, especially with uncertainties in harringtonine pharmacokinetics (***Aguilera et al., 2019***) or RQC-mediated termination events (***Latallo et al., 2023***; ***Goldman et al., 2021***).

Outlook

An important contribution of our work is providing an initial framework for modeling translation kinetics at the single-trace level. Currently, this approach is tractable for run-off assays, where mRNAs eventually deplete their ribosomes, simplifying parameter estimation. Although challenging, extending the model beyond harringtonine assays would circumvent these limitations, while giving insights on initiation regulation, including bursting. This could be done by extending the model to steady-state translation and incorporating a 2-state telegraph model to capture "bursty" initiation. Furthermore, introducing constructs with different 5'UTRs, similar to the work of (***Livingston et al., 2023***), would provide valuable insights into how bursting dynamics interact with elongation rates. In addition, the current model infers population level parameters while accounting for single-trace stochasticity, extending the model (hierarchically) to allow for transcript-specific rates or stalling could provide valuable insights.

Addressing the current limitations, including the influence of RQC on run-off kinetics and the non-exponential distribution of termination events, will further refine our understanding of translation dynamics and improve model accuracy. In parallel, integrating run-off and bursting traces within a unified framework and incorporating transcript-specific kinetic parameters should offer a more complete picture of how cells regulate translation at the single-mRNA level. The latter

could potentially be achieved by replacing the HMM with a particle-filter approach, to infer single-transcript kinetics ***Wills and Schön*** (***2023***). Finally, exploring the molecular mechanisms underlying the observed coupling of initiation and elongation, as well as the functional significance of bursting dynamics and ribosome density regulation, will be critical for unraveling how cells maintain proteostasis under diverse physiological and stress conditions.

Methods and Materials

Experimental Design

Model system and cell culture

We used a cell line derived from the HeLa-11ht cell line generated by Weidenfield et al. (***Weidenfeld et al., 2009***) which contains a site for Flp-RMCE (recombinase-mediated cassette exchange), allowing a single-copy genomic integration of a target gene, and constitutively expressing the reverse tetracycline-controlled transactivator (rtTA2-M2) for inducible expression. The cell line was further engineered to stably express GFP-tagged single-chain antibodies (scFv-GFP) against GCN4, and NLS-stdMCP-stdHalo-RH1 fusion protein (***Voigt et al., 2017***) (courtesy of Jeffrey Chao Lab, FMI Basel). The MCP protein recognizes a MS2 stem-loop cassette in the 3′ UTR of the reporter mRNA, while the RH1 domain associates with actin filaments through the interaction with the MyosinVa molecular motor allowing stable imaging of actin-anchored mRNAs (***Figure 1***A). In the following we refer to this cell line as the parental cell line, from which we obtain monoclonal cell lines expressing the SunTag reporters by stable transfection and fluorescence-activated cell sorting (FACS).

HeLa cells are cultured in Dulbecco's Modified Eagle Medium (DMEM) containing 4.5 g/L glucose, Penicillin (100 U/ml), Streptomycin (100 µg/ml), L-Glutamine (4 mM) and 10% fetal bovine serum (FBS). Cells are maintained at 37°C and 5% CO2. For transient and stable transfections, we use Fugene HD Transfection Reagent (Promega) with Opti-MEM reduced serum medium (Thermo Fisher Scientific) according to the manufacturer's instructions.

To perturb eIF5A activity, cells are treated with 1 µM N1-guanyl-1,7-diaminoheptane (GC7) for 24h before imaging. Because GC7 is known to be inactivated by the action of amine oxidases, which are abundant in serum, we add 1 mM aminoguanidine (AG) to inhibit amine oxidases, as is typically done in the literature (***Maier et al., 2010***). The control sample is treated with AG only.

DNA constructs

All the constructs described in this project are obtained from the previously described SunTag-Renilla-MS2 plasmid (***Wilbertz et al., 2019***) (Addgene plasmid #119945, ***Figure 1***A) via restriction-free cloning. The resulting plasmids contain SunTag (24 x GCN4), destabilized FKBP domain (***Banaszynski et al., 2006***) with a stop codon and a 24xMS2 stem-loop cassette. In addition, PPG contains a subsequence of Human collagen type I α1 (transcript COL1A1-201, from nucleotide 2619 to 3672, 1056 nt), while AAG contains the same subsequence where all proline amino acids (24% of the total amino acid content) are mutated to alanine, maintaining the same codon adaptation index (***Figure 1***B).

SunTag-Renilla-RH1-MS2 is a plasmid containing the RH1 domain at the C-terminus of the Renilla open reading frame (***Voigt et al., 2017***) and it was used in the calibration experiment to image the mature proteins.

Cell line generation

$3 \cdot 10^5$ HeLa cells are seeded into a 6-well plate and the next day transfected with 2 µg of the FLPe recombinase plasmid (Addgene #20733) together with 2 µg of the plasmid carrying the SunTag reporter flanked by Flp-recombinase target sites. The next day, 5 µg/ml puromycin (Invivogen) is added to select for transfected cells. Two days later, the puromycin-containing medium is removed and cells are kept in growth medium containing 50 µM ganciclovir (Sigma-Aldrich) for 10 days to select for cells with successful RMCE. Single clones are isolated in a 96-well plate via FACS, based on

cytoplasmic GFP intensity. Clones with moderate GFP background and responsive to doxycycline induction are selected for expansion.

Transient transfection

For the calibration experiment cells are transiently transfected with SunTag-Renilla-RH1-MS2 plasmid. Cells are seeded at $7.5 \cdot 10^3$ cells/well in a 8-well glass-bottom µ-slide (170 µm, ibidi) 48h before imaging. After 24h cells are transfected with Fugene transfection reagent according to the manufacturer's instructions with the SunTag plasmid but without the FLPe recombinase plasmid.

Generation of eIF5A knock-out cell line

Starting from the cell line stably expressing PPG, we generate an eIF5A knock out (KO) line using the single-guide RNA reported by Manjunath et al. (***Manjunath et al., 2019***) (eIF5A sgRNA #1 5' – AGAGGACCTTC GTCTCCCTG – 3') in an all-in-one Cas9-GFP plasmid. Single clones are selected with FACS sorting based on GFP intensity. Three clones are selected for further expansion, genotyping of the target site and western blotting of eIF5A and h-eIF5A. The clone with the strongest reduction in total eIF5A is chosen for imaging.

Live-cell imaging

Wild-type cells are seeded at a concentration of $7.5 \cdot 10^3$ cells/well in a 8-well glass-bottom µ-slide (170 µm, ibidi) 48h before imaging. eIF5A knock-out cells are seeded at $15 \cdot 10^3$ to reach a similar confluency at the acquisition. For the experiments involving GC7 treatment, 24h before imaging the growth medium is replaced with fresh medium supplemented with 1 mM AG in the control wells and with 1 µM GC7 and 1 mM AG in the treated wells. For experiments involving the eIF5A knock-out, the growth medium is replaced with fresh medium (without AG). Before imaging the growth medium is replaced with fresh medium containing 1 µg/ml doxycycline (DOX) in order to induce the transcription of reporter mRNAs. After 40 minutes, the medium is further supplemented with Janelia Fluor 640 HaloTag ligand (JF646) (Promega), at 100 nM final concentration. After 20 minutes of incubation, the medium is removed and cells were washed in PBS. Cells are then kept in FluoroBrite DMEM (Thermo Fisher Scientific) supplemented with 10% FBS and 4 mM L-glutamine for 40 min before imaging and during the acquisition.

Cells are imaged using a spinning-disk confocal microscope (Visitron Spinning Disk CSU W1) equipped for live-cell imaging. Images are acquired using Visiview (Visitron) as single planes every 20 seconds and for 90 minutes, with 100 ms exposure time, 60X objective and hardware autofocus (see ***Table 1*** for technical specifications). The focus is always set 0.8 µm away from the coverslip, yielding a focal plane close to the plasma membrane, ventral side of the cell. Because of the actin cortex, this area is usually rich in tethered reporter mRNAs. Cells are imaged sequentially in GFP and Cy5 channels with a single EMCCD camera.

In run-off assays harringtonine (HT) (Cayman Chemical) is pre-diluted in FluoroBrite and added to the cells (final concentration 3 µg/ml) mounted on the microscope stage. In practice, we add 53 µL of 20 µg/ µL working solution to 300 µL of FluoroBrite medium, pipetting up and down three times to ensure mixing. Image acquisition is started 30s – 60s after treatment (the delay between treatment and imaging is recorded for each acquisition). Time points are acquired every 20 s.

Laser power measurement and flat-field correction

488 nm and 640 nm laser power is measured at the beginning of each experiment using a power meter and a 10X Air objective (0.4 NA). During each acquisition – except in the calibration experiment – the percentage of laser power used is set to match 0.68 mW for the 488 nm laser and 2.5 mW for the 640 nm laser.

Every two months both microscope flat field and dark current are measured. For the flat-field measurement a uniformly fluorescent sample is prepared using ATTO 488 (AD 488-21, Atto-Tech) and ATTO 647 (AD 647-21, Atto-Tech), both in free acid form. Both dyes are dissolved in water

at 1mM concentration (ATTO 647 dissolves inefficiently and the procedure can be improved by considering a different solvent) and then filtered with a 0.2 µm filter to remove aggregates. The solutions are added to 2% agarose gel to obtain a final concentration of 10 µM. The two fluorescent solutions are mixed 1:1 and a 40 µL drop is added to a microscopy slide and covered with a 22 x 22 mm coverslip, creating a thin, uniformly fluorescent, agarose layer. After drying, 20 xy positions are acquired in both channels with the 60X oil objective. The final flat-field image is obtained by averaging the 20 images and applying a median filter with radius 5 pixels. For the dark field measurement 100 time points are acquired without laser and without any specimen in both channels, and averaged to obtain the dark current image.

Mature protein intensity measurement

To measure the intensity of one mature protein (24 GFP molecules) we use a SunTag-Renilla-RH1-MS2 reporter with an RH1 domain at the end of the coding sequence for actin-tethering of mature proteins (***Voigt et al., 2017***). The cells are seeded and prepared for imaging as previously described, except that DOX incubation is shortened to 20 min to avoid overcrowding of mature proteins in the cytoplasm. Prior to imaging, cells are treated with 100 µg/ml of puromycin (Sigma-Aldrich) to disassemble translating ribosomes, then imaged at 100% power (4.63 mW measured with a 10X Air objective) for 100 s at 10 Hz (***Figure 1—figure Supplement 2***A). Spot detection, tracking and intensity quantification (***Figure 1—figure Supplement 2***B) are performed in the GFP channel only, since mature proteins do not colocalize with the mRNA signal. The intensity of each spot is averaged over the 100 frames.

To build the intensity-power calibration curve, cells are treated with cycloheximide (Sigma-Aldrich) at 200 µg/ml final concentration 5 minutes before imaging, to block the ribosomes and have constant GFP intensity per mRNA molecule. Cells are imaged at 20%, 40%, 60%, 80% and 100% power, in rapid succession (10 frames per laser power at 0.5 Hz). This procedure revealed a linear relationship between the spot intensity and laser power (***Figure 1—figure Supplement 2***C), allowing us to infer the mature protein intensity at the laser power used for live imaging, from the value measured at 100% laser power. The final estimate (14 $\pm$ 2 a.u.) allows us to estimate the average number of ribosomes translating each report (***Figure 1—figure Supplement 2***D).

Quantification of Intensity Traces

Image processing

The live-cell images acquired during experiments are corrected for flat field and dark current as follows

$$C = \frac{O - DC}{FF - DC} \langle FF - DC \rangle \tag{1}$$

where C is the corrected image, O is the original image, DC is the dark current image, FF is the flat field image and the average $\langle\ \rangle$ is calculated over all the pixels. Each experiment is corrected with the most recent dark current and flat-field images up to that date. Both the dark current and the flat-field measurements are very consistent across several months of imaging.

Spot tracking and intensity quantification

The spot detection is performed in the far red channel with TrackMate 7 (Fiji) (***Ershov et al., 2022***). Nuclei were excluded from detection because of the very high background due to JF646 nuclear localization. The tracking is performed using the TrackMate simple Linear Assignment Problem (LAP) tracker, with a maximal linking distance of 2 µm, a maximal distance for gap-closing of 3 µm and a maximal frame interval between two linked spots of 2 frames. The minimal track length is set to 5 minutes.

Given a 2 µm $\times$ 2 µm region around an mRNA, the intensity of the spots in the far red and green channel is inferred using Bayesian inference. The spot intensity in each channel is approximated

as a 2D gaussian:

$$\mu_{2D}(x, y) = \frac{I}{2\pi w^2} \exp\left(-\frac{(x - x_0)^2}{2w^2} - \frac{(y - y_0)^2}{2w^2}\right) + g(x, y) \tag{2}$$

where I is the total spot intensity, w is the width of the spot, x_0 and y_0 are the coordinates of the spot center in micrometer units and $g(x, y)$ is a background given by

$$g(x, y) = c + b(y - y_0) + a(x - x_0), \tag{3}$$

with $a, b, c \in \mathbb{R}$. Hence, the background is modeled as a 2D plane with a and b representing the tilt in the x and y directions, respectively. This choice allowed us to model local changes in the cytoplasmic background, such as those happening when a spot is close to the cell membrane, and the GFP background is higher inside the cell than outside. Both a, b and c are parameters of the model. Finally, the intensity of a pixel is modeled as

$$i(x, y) \sim \text{Normal}\left(\mu_{2D}(x, y), \sigma\right) \tag{4}$$

where σ is the standard deviation and it is estimated as the pixel standard deviation in the cytoplasmic background, and its value is fixed during the inference.

The priors on x_0 and y_0 are centered on the position x_r, y_r of the red spot, as given by TrackMate:

$$\begin{aligned} x_0 &\sim \text{Normal}(x_r, 0.2) \\ y_0 &\sim \text{Normal}(y_r, 0.2) \end{aligned} \tag{5}$$

with a standard deviation of 0.2 µm approximately corresponding to the average distance between the mRNA spot and the translation spot. The prior on the spot size is very peaked for regularization purposes

$$w \sim \text{InvGamma}(\mu = 0.20, \sigma = 0.02). \tag{6}$$

The prior on the total intensity I is an "uninformative" prior

$$I \sim \text{HalfNormal}(\sigma = 1000). \tag{7}$$

The background $g(x, y)$ is a 2D-plane, with

$$c \sim \text{Normal}(\mu_c, \sigma_c) \tag{8}$$

where μ_c and σ_c are input parameters shared among all acquisitions, and they are estimated as the average and the standard deviation of the cytoplasm intensity across different cells and different experiments. Finally,

$$a, b \sim \text{Normal}(0, 50) \tag{9}$$

which we include to account for the background variation when a spot is close to the transition between the cell interior and exterior. For the calibration experiment described in Mature protein intensity measurement, all the steps (detection, tracking and quantification) are done exclusively in the green channel, since mature proteins do not co-localize with the mRNA signal.

The inference is performed with the Hamiltonian Monte Carlo algorithm implemented in Stan (***Team, 2024***) through the PyStan Python interface.

Preprocessing and data filtering

The estimated spot intensity is affected by tracking errors and diffusion of the mRNA in the z direction of the focal plane. Cycloheximide (CHX) traces – acquired in the same imaging conditions as in Live-cell imaging – are used to estimate this noise and partially correct experimental traces. After regressing out the linear decay due to photobleaching, the standard deviation of the signal is calculated relative to the mean intensity of the trace; averaging over 236 traces yields a global estimate of the multiplicative noise (see ***Figure 2—figure Supplement 1*** for examples of CHX traces and autocorrelation).

Next, all traces are smoothed with a low-pass filter (Butterworth filter), with a 1/120 Hz cut-off. At each time point the relative difference between the raw and smoothed trace is calculated; if this relative difference is higher than twice the multiplicative noise calculated from cycloheximide traces we replace it with the smoothed value. In practice, this corresponds to spikes or drops larger than $\sim 50\%$ of the smoothed intensity.

For the run-off experiments the analysis is restricted to traces that start no later than 100 s after HT is added to the medium, so that translation is initially "close" to the distribution in the absence of inhibitor, considering that HT takes ~ 60 s to enter the cells and be effective (***Ingolia et al., 2009***). Experiments with less than 10 traces in the control or in the perturbed (GC7/KO) conditions are excluded from the analysis. In addition, two acquisitions exhibited a delayed onset of translation, questioning the effectiveness of HT treatment in those instances, and were also excluded.

Mathematical models

Bayesian modeling of run-off traces

We consider a set of intensity traces $y_{r,t}$, where r is a trace index and t is a discrete time index, which is a multiple of the time step dt. We assume a common underlying stochastic process that can be described by an initiation rate α and an average elongation rate λ of the ribosomes along the transcript. In particular, we use a Hidden Markov Model (HMM) in which each trace $y_{r,t}$ is a noisy observation of a discrete Markov chain $N_{r,t}$, where $N_{r,t}$ is the number of translating ribosomes on the transcript r at time t. The inference is performed in Stan using a Markov chain Monte Carlo algorithm called Hamiltonian Monte Carlo (HMC). It uses an approximate Hamiltonian dynamics simulation based on numerical integration which is then corrected by performing a Metropolis acceptance step (***Betancourt and Girolami, 2013***).

In the following we describe how we derive the expressions of the initial state probability and the transition probabilities from a simple mean-field approximation of the ℓ-TASEP under the assumption of low ribosome density. At the end of the section we describe our assumptions related to the emission probability, i.e. the probability of observing the noisy signal y given the hidden state N.

Given a transcript of size L, we define the average ribosome density ρ, defined as the average fraction of transcript occupied by the ribosomes

$$\rho := \frac{\langle N \rangle \ell}{L}, \tag{10}$$

where ℓ is the length of transcript occupied by one ribosome and $\langle N \rangle$ is the average number of ribosomes on the transcript. The latter can be expressed as the product between the current J (number of particles per transcript site and per unit of time, equivalent to the protein synthesis rate) and the average residence time L/λ. Hence, ***Equation 10*** can be written as

$$\rho = J \frac{\ell}{\lambda}. \tag{11}$$

In the initiation-limited regime as described in the continuum-limit approximation by ***Erdmann-Pham et al.*** (***2020***), the current is mainly determined by the initiation rate and it is given by

$$J = \alpha \frac{\lambda - \alpha}{\lambda + (\ell - 1)\alpha}. \tag{12}$$

In our model we assume that the initiation rate is low compared to elongation and ribosome excluded volume interactions can be neglected. In this case, we can expand the expression of J as a function of the ratio α/λ:

$$J = \alpha \left\{ 1 - \ell \frac{\alpha}{\lambda} + o\left[\left(\ell \frac{\alpha}{\lambda} \right)^2 \right] \right\}, \tag{13}$$

to observe that when $\ell \frac{\alpha}{\lambda} \ll 1$, or equivalently $\lambda/\alpha \gg \ell$, we can approximate $J \approx \alpha$ and

$$\rho \approx \frac{\alpha}{\lambda} \ell \quad \text{if } \lambda/\alpha \gg \ell, \tag{14}$$

an approximation that we will use throughout our model. The initial state probability $\Theta_r(N)$ is the probability of observing N ribosomes at the beginning of trace r, given the model parameters. We set $t = 0$ when the run-off starts and we assume that this happens 60 s after HT is added to the medium (***Ingolia et al., 2011***). At $t = 0$ we can assume that the number of ribosomes N on the transcript is given by a Poisson distribution with mean $\alpha L/\lambda$, as in the absence of inhibitor, and where the low-density approximation in ***Equation 14*** is assumed (***Szavits-Nossan and Grima, 2023***). Given that trace r starts at time $t_r \geq 0$, we assume that the ribosome distribution has not yet been substantially altered by initiation inhibition, and we approximate it by a Poisson distribution with mean corrected by t_r

$$p_r(N \mid \alpha, \lambda) = \text{Poisson}\left(N \,\middle|\, \alpha\left(\frac{L}{\lambda} - t_r\right)\right). \tag{15}$$

However, the probability of having $N = 0$ ribosomes on the transcript, hence the probability that a transcript is inactive at the time of HT treatment, may not follow the Poisson distribution – for instance, in the presence of switching between active and inactive states (whether or not the Poisson distribution is still a valid description for $N > 0$ will depend on the switching rates) (***Szavits-Nossan and Grima, 2023***). In practice, we describe the probability for a trace to be inactive as p_{off}, which is a parameter of the model and it is shared among all traces. Finally, the initial probability vector for trace r is given by

$$\Theta_r(N \mid \alpha, \lambda, p_{\text{off}}) = \begin{cases} p_{\text{off}} & N = 0 \\ p_r(N) \,/\, (1 - p_r(0)) & N > 0. \end{cases} \tag{16}$$

By choosing such a Poisson distribution, we assume that, in case of bursting, the durations of active and inactive periods are longer than the total mRNA translation time. For the inference we need to fix the maximum number of ribosomes $N_{\max}$ that can be translating the mRNA. We fix $N_{\max} = 100$, which corresponds to a density $\rho \approx 0.94$ for $L = 1066$ aa and $\ell = 10$ aa.

The transition probability $\Gamma(N \mid N', \alpha)$ is the probability of jumping from N' to N in a time dt, given the kinetic parameters α. Because at $t \geq 0$ initiation is inhibited, the only possible transitions are those satisfying $N \leq N'$, hence termination events.

When $\lambda/\alpha \gg \ell$ the waiting time distribution between successive termination events was derived in ***Szavits-Nossan and Grima*** (***2023***) and reads

$$P_{\text{term}}(t) = \alpha \frac{\lambda - \alpha}{\lambda - 2\alpha}\left(e^{-\alpha t} - e^{-(\lambda-\alpha)t}\right). \tag{17}$$

Since we are assuming $\alpha \ll \lambda/\ell < \lambda$ we can say that $\frac{\lambda-\alpha}{\lambda-2\alpha} \approx 1$ and $e^{-(\lambda-\alpha)t} \ll e^{-\alpha t}$. As a consequence, ***Equation 17*** is approximately equal to the waiting time distribution between initiation events:

$$P_{\text{term}}(t) \approx \alpha e^{-\alpha t}. \tag{18}$$

So, we can define the transition probability from N to $N - k$ given α as

$$\Gamma(N - k \mid N, \alpha) = \text{Poisson}(k \mid \alpha dt). \tag{19}$$

For the inference, we need to set a maximum number of termination events $k_{\max}$ per time step dt. Considering that the initiation rates measured in the literature with similar systems range from less than 1 ribosome per min up to 5 ribosomes per min(~ 0.08 s^{-1}) (***Boersma et al., 2019***; ***Livingston et al., 2023***), we fixed $k_{\max} = 6$, since the probability of 6 initiation events in dt with $\alpha = 0.08$ s^{-1} is about 0.005.

We assume that the emission probability $\Phi(y \mid N, t)$ – the probability of observing an intensity y given N ribosomes at time t – is lognormal

$$\Phi(y \mid N, t) = \frac{1}{y\, s(t)\sqrt{2\pi}} \exp\left\{-\frac{[\ln y - \ln \mu(N, t)]^2}{2 s^2(t)}\right\} \tag{20}$$

to account for different sources of noise arising during acquisition and not filtered by the intensity quantification and pre-processing steps (***Wildner et al., 2023***). These sources include z-diffusion of

the mRNA, irregular background, fluctuations in laser intensity, photon shot noise, etc. In addition, this choice aims to effectively describe the noise deriving from the uncertainty regarding the ribosome distribution along the mRNA. For a time t and N ribosomes, an equivalent representation in terms of random variables is

$$Y = \mu \exp(sX) \tag{21}$$

where X is a standard normal random variable, $\mu := \mu(N,t)$ and $s := s(t)$. In practice, the measured spot intensity y is given by the true signal μ multiplied by an exponentially-transformed gaussian noise.

The following discussion is dedicated to the derivation of $\mu(N,t)$ and $s(t)$ which explains the explicit dependence of the emission probability on time. Notice that the noise parameter s can be expressed in terms of the expectation $\langle\, y(N,t)\,\rangle$ and variance $\sigma_y^2(N,t)$ of y as

$$s^2(N,t) = \ln\left(1 + \frac{\sigma_y^2(N,t)}{\langle\, y(N,t)\,\rangle^2}\right). \tag{22}$$

The denoised signal μ is a function of the number of translating ribosomes N and time t and, since we are neglecting the precise ribosome positions along the mRNA, it is an average over all the possible configurations $\mathcal{C}_{N,t}$ of N ribosomes along the mRNA at time t of run-off. In practice, we consider that the ribosomes are uniformly distributed along the mRNA. We express it as

$$\mu(N,t) = \left\langle\, I(\mathcal{C}_{N,t})\,\right\rangle_{\mathcal{C}_{N,t}} = b_0 + \gamma(t) N i_{\mathrm{MP}}, \tag{23}$$

where $I(\mathcal{C}_{N,t})$ is the intensity generated by the ribosome configuration $\mathcal{C}_{N,t}$, b_0 is the offset, i_{MP} is the intensity of one mature protein and γ is a time-dependent correction factor that accounts for the fact that ribosomes translating the SunTag have intensity smaller than i_{MP}. It depends on time because during run-off the ensemble of possible ribosomes configurations along the mRNA changes, as ribosomes progress on the transcript. Given the length of the SunTag L_S, we can express $\gamma(t)$ in terms of the elongation rate λ (see Mean intensity correction factor during run-off for the full derivation):

$$\gamma(t) = 1 - \frac{(L_S - \lambda t)^2}{2L_S(L - \lambda t)} \quad \text{for } \lambda t \leq L_S, \tag{24}$$

which agrees with the result for $t = 0$ previously reported (***Aguilera et al., 2019***). When all ribosomes have completed the translation of the SunTag, and approximately for $\lambda t > L_S$, $\gamma(t) = 1$. The value of γ over time agrees well with simulation results over a broad range of ribosome densities (***Figure 2***C and ***Figure 2—figure Supplement 2***A).

We can compute the variance of the total spot intensity in a similar way

$$\sigma^2(N,t) := \mathrm{Var}\left[I(\mathcal{C}_{N,t})\right]_{\mathcal{C}_{N,t}} = \nu(t) N i_{\mathrm{MP}}^2 \tag{25}$$

where ν is given by (see Intensity variance for the derivation)

$$\nu(t) = \frac{1}{L - \lambda t}\left(L - \frac{2L_S}{3} - \frac{(\lambda t)^3}{3L_S^2}\right) - \left(1 - \frac{(L_S - \lambda t)^2}{2L_S(L - \lambda t)}\right)^2. \tag{26}$$

The agreement with simulations is good at low densities, while it significantly deteriorates at higher densities (***Figure 2***D and ***Figure 2—figure Supplement 2***A). This is expected as the expressions of both $\gamma(t)$ and $\nu(t)$ are derived under the assumption that the ribosome density is sufficiently low that excluded-volume interactions can be neglected, and the probability to find a ribosome at position i can be approximated by N/L.

We can write the total variance $\sigma_y^2(N,t)$ of the signal $y(N,t)$ as the sum of the variance σ_{meas}^2 due to measurement noise and variance $\sigma_C^2(N,t)$ due to the ribosome configurations on the mRNA, and effectively subsume both of them under the log-normal noise. So, the observed intensity y is a

random variable because of the unknown measurement process and because of the unknown underlying ribosome distribution. Then, the normalized variance in the expression of s (***Equation 22***) reads

$$\frac{\sigma_y^2(N,t)}{\langle\, y(N,t)\,\rangle^2} = \frac{\sigma_{\text{meas}}^2(N,t)}{\langle\, y(N,t)\,\rangle^2} + \frac{\sigma_{\mathcal{C}}(N,t)^2}{\langle\, y(N,t)\,\rangle^2} \tag{27}$$

where the average is intended over the measurements and the configurations $\mathcal{C}_{N,t}$. We approximate the first term in the sum as

$$\frac{\sigma_{\text{meas}}^2(N,t)}{\langle\, y(N,t)\,\rangle^2} \approx \frac{\sigma_{\text{meas}}^2(N,t)}{\left\langle\, I(\mathcal{C}_{N,t})\,\right\rangle_{\text{meas}}^2} \tag{28}$$

where the average on the right-hand side is performed over the measurements and where we assume that the right-hand side is a constant multiplicative noise that does not depend on the specific ribosome configuration, nor the intensity, and subsumes the uncertainty in the acquisition process. We approximate the second term in the sum as

$$\frac{\sigma_{\mathcal{C}}^2(N,t)}{\langle\, y(N,t)\,\rangle^2} \approx \frac{\sigma^2(N,t)}{\left\langle\, I(\mathcal{C}_{N,t})\,\right\rangle_{\mathcal{C}_{N,t}}^2} = \frac{\sigma^2(N,t)}{\mu^2} = \frac{1}{N}\frac{\nu(t)}{\gamma^2(t)} \tag{29}$$

and, by substituting N with the average $\langle\, N\,\rangle = \alpha L/\lambda$,

$$\frac{\sigma_{\mathcal{C}}^2(N,t)}{\langle\, y(N,t)\,\rangle^2} \approx \frac{\lambda}{\alpha L}\frac{\nu(t)}{\gamma^2(t)}. \tag{30}$$

Finally, we can use ***Equation 22*** to write the final estimate for s

$$s(t) = \sqrt{\ln\left(1 + \frac{\sigma_{\text{meas}}^2}{\langle I\,\rangle_{\text{meas}}^2} + \frac{\lambda}{\alpha L}\frac{\nu(t)}{\gamma^2(t)}\right)}, \tag{31}$$

where we have omitted the dependence of I on ribosome configurations $\mathcal{C}_{N,t}$ for simplicity. Notice that $s(t)$ depends solely on time and on the kinetic parameters α and λ. When there are no ribosomes on the transcript or when $\nu(t) = 0$ (all ribosomes have terminated the translation of the SunTag) the noise is simply given by

$$s_0 := \sqrt{\ln\left(1 + \frac{\sigma_{\text{meas}}^2}{\langle I\,\rangle_{\text{meas}}^2}\right)}. \tag{32}$$

Finally, the emission probability is given by

$$\Phi\,(y \mid N,t) = \frac{1}{ys(t)\sqrt{2\pi}}\exp\left\{-\frac{[\ln y - \ln\mu(N,t)]^2}{2s^2(t)}\right\} \tag{33}$$

where $\mu(N,t)$ is given by ***Equation 23*** and $s(t)$ is given by ***Equation 31***.

For each experiment we estimate the traces baseline b_0 in ***Equation 23*** and the term $\sigma_{\text{meas}}^2/\langle I\,\rangle^2$ in ***Equation 31*** independently of the other model parameters. The offset b_0 is estimated as the average intensity of the untranslated traces: because it is very consistent across experiments and conditions we fix it to its average value across experiments, b_0 = 6 a.u.

The term $\sigma_{\text{meas}}^2/\langle I\,\rangle^2$ determines the noise parameter s_0 (***Equation 32***), which accounts for the measurement noise alone (and not for the uncertainty of the ribosome distribution). It is estimated independently for each experiment (all conditions together) by calculating the variance of untranslated traces σ_{meas}^2 divided by the mean intensity squared of the trace $\langle\, I\,\rangle^2$. The values obtained in this way correspond to s_0 ranging from 0.31 to 0.38, with mean 0.34 and standard deviation 0.02 – across experiments. In an independent estimate from raw CHX traces described in Preprocessing and data filtering, we obtain $s_0 = 0.36$, a value comparable to what was obtained for untranslated traces (***Figure 2—figure Supplement 1***A, B).

Mean intensity correction factor at $t = 0$

We compute here the correction factor γ for the total intensity of N ribosomes used in Bayesian modeling of run-off traces, at $t = 0$. The number of epitopes n on the SunTag as a function of the position x can be approximated as

$$n(x) = \frac{n_S}{L_S - 1}(x - 1) \quad x \leq L_S \tag{34}$$

where $n_S = 24$ is the total number of epitopes encoded in the SunTag and L_S is the SunTag length. For $x > L_S$ we have $n(x) = n_S$. In the following we will consider the intensity normalized by i_{MP} and use the fraction of epitopes $f(x) := n(x)/n_S$. We can compute the average intensity for $N = 1$ ribosomes translating the SunTag as

$$\mu_1 = \sum_{x=1}^{L} f(x)p(x) \tag{35}$$

where $p(x)$ is the probability of finding a ribosome at x. After approximating $p(x) = 1/L$ and using the definition of $f(x)$ we have

$$\mu_1 = \frac{1}{L}\sum_{x=1}^{L} f(x) = \frac{1}{L}\left[\frac{1}{L_S - 1}\sum_{x=1}^{L_S}(x-1) + (L - L_S)\right]$$

which yields

$$\mu_1 = 1 - \frac{L_s}{2L} = \gamma, \tag{36}$$

where we used

$$\sum_{x=1}^{L_S}(x-1) = \frac{L_S(L_S - 1)}{2}.$$

For $N > 1$ we have $\mu_N = N\mu_1 = N\gamma$.

Mean intensity correction factor during run-off

We compute here the correction factor γ for the total intensity of N ribosomes used in Bayesian modeling of run-off traces during run-off. While ribosomes run off the transcripts, the proportion of ribosomes on the SunTag changes, which can be taken into account by a time-dependent correction factor $\gamma(t)$, dependent on the elongation rate λ (that we assume to be uniform along the transcript). We can approximate the occupation probability as

$$p(x \mid N, t) = \begin{cases} 0 & \forall x \leq x_t \\ N/(L - x_t) & \forall x > x_t \end{cases} \tag{37}$$

where we defined $x_t := \lfloor \lambda t \rfloor \in [1, L]$, the average distance covered by the ribosomes in a time t. With the same algebra as before we get $\mu_N = N\gamma(t)$ with

$$\gamma(t) = \frac{1}{L - x_t}\left(L - \frac{L_S}{2} - \frac{x_t(x_t - 1)}{2(L_S - 1)}\right) \simeq 1 - \frac{(L_S - \lambda t)^2}{2L_S(L - \lambda t)} \quad \forall t \leq L_S/\lambda \tag{38}$$

else $\gamma(t) = 1$.

Intensity variance

We compute the variance $V_1(y)$ of the intensity y produced by $N = 1$ ribosomes at time t during run-off, in units of i_{MP}^2 ($t = 0$ corresponds to when run-off starts). The variance for N ribosomes will be the sum of the variances: $V_N(y) = NV_1(y)$. We can write the variance as

$$V_1(y) = \langle\, y^2 \,\rangle - \mu_1^2 \tag{39}$$

with μ_1 given by ***Equation 36*** and

$$\langle\, y^2 \,\rangle = \sum_{x=x_t}^{L} f(x)^2 p(x) = \frac{1}{L - x_t}\left(\sum_{x=1}^{L} f(x)^2 - \sum_{x=1}^{x_t} f(x)^2\right) \tag{40}$$

where $x_t := \lfloor \lambda t \rfloor \in [1, L]$ as before. The first summation gives

$$\begin{aligned}\sum_{x=1}^{L} f(x)^2 &= \frac{1}{(L_S-1)^2}\sum_{x=1}^{L_S}(x-1)^2 + L - L_S \\ &= \frac{1}{(L_S-1)^2}\left(\frac{L_S(L_S+1)(2L_S+1)}{6} - L_S(L_S+1) + L_S\right) + L - L_S \\ &= \frac{L_S(2L_S-1)}{6(L_S-1)} + L - L_S \approx L - \frac{2L_S}{3}.\end{aligned}$$

The second term

$$\begin{aligned}\sum_{x=1}^{x_t} f(x)^2 &= \frac{1}{(L_S-1)^2}\sum_{x=1}^{x_t}(x-1)^2 \\ &= \frac{1}{(L_S-1)^2}\left(\frac{x_t(x_t+1)(2x_t+1)}{6} - x_t(x_t+1) + x_t\right) \\ &= \frac{x_t(2x_t-1)(x_t-1)}{6(L_S-1)^2} \approx \frac{(\lambda t)^3}{3L_S^2}.\end{aligned}$$

Finally,

$$\langle\, y^2 \,\rangle \approx \frac{1}{L-\lambda t}\left(L - \frac{2L_S}{3} - \frac{(\lambda t)^3}{3L_S^2}\right).$$

The final results is then

$$V_1(y) = \frac{1}{L-\lambda t}\left(L - \frac{2L_S}{3} - \frac{(\lambda t)^3}{3L_S^2}\right) - \left(1 - \frac{(L_S-\lambda t)^2}{2L_S(L-\lambda t)}\right)^2. \tag{41}$$

Simulation of SunTag traces

SunTag traces are obtained *in silico* by simulating the homogeneous ℓ-TASEP with the Gillespie algorithm (***Gillespie, 1976***). The algorithm is formulated for a general set of site-specific elongation rates λ_i, but for the purposes of this study we simulate a homogeneous system with all elongation rates equal to λ; for simplicity, the termination rate λ_{L-1} is considered equal to the elongation rate. We first describe the algorithm used for the ℓ-TASEP simulations without bursting, and then we describe its generalization for a bursting initiation.

The simulation starts at $t = 0$. At any step of the simulation, a vector $\boldsymbol{\tau} = (\tau_0, \dots, \tau_{L-1}) \in \{0,1\}^L$ specifies the ribosome occupancy state of the mRNA (of length L) and a list Ω specifies all the possible reactions and their associated time. In particular, $\omega_k \in \Omega$ is a list of two elements: $\omega_k[0] \in \{0, \dots, L-1\}$ specifies the event and $\omega_k[1] \in \mathbb{R}^+$ its time of occurrence. $\omega_k[0] = -1$ corresponds to an initiation event, $\omega_k[0] = L-1$ a termination event, and $\omega_k[0] \in \{0, \dots, L-2\}$ an elongation event at position $\omega_k[0]$. The list Ω is kept ordered according to the time of occurrence, such that the first element of the list is the one occurring earlier in time and $\omega_k[1] \le \omega_{k+1}[1]$. In the following $\mathrm{Exp}(\lambda)$ is the exponential distribution with scale parameter λ.

1. Remove the event ω_1 from Ω (let $i = \omega_1[0]$ and $dt = \omega_1[1]$).
2. Update the total time $t \leftarrow t + dt$ and the single events time $\omega_k[1] \leftarrow \omega_k[1] - dt\ \forall k$.
3. Update the occupancy state:
   (a) If $i = -1$ (initiation), then set $\tau_0 = 1$.
   (b) If $i = L-1$ (termination), then set $\tau_{L-1} = 0$.
   (c) If $i \in \{0, \dots, L-2\}$ (elongation), then set $(\tau_i, \tau_{i+1}) \leftarrow (0, 1)$.
4. Find possible new reactions and sample their associated times:
   (a) If $i = L-1$ and $\tau_{L-\ell-1} = 1$, then sample $t_0 \sim \mathrm{Exp}(\lambda_{L-\ell-1})$ and insert $(L-\ell-1, t_0)$ into Ω.
   (b) If $i \in \{0, \dots, L-2\}$
      i. If $i = \ell - 1$, then sample $t_0 \sim \mathrm{Exp}(\alpha)$ and insert $(-1, t_0)$ into Ω.

ii. If $i > \ell - 1$ and $\tau_{i-\ell} = 1$, then sample $t_0 \sim \mathrm{Exp}(\lambda_{i-\ell})$ and insert $(i-\ell, t_0)$ into Ω.

iii. If $i < L - \ell$ and $\tau_{i+\ell+1} = 0$ or if $L - \ell \leq i \leq L - 2$, then sample $t_0 \sim \mathrm{Exp}(\lambda_{i+1})$ and insert $(i+1, t_0)$ into Ω.

5. Go to 1.

The algorithm easily generalizes to a 2-state telegraph model for initiation: the state of the system is now described by $\boldsymbol{\tau}$ and $G \in \{0, 1\}$, with $G = 0$ if the transcript is inactive and $G = 1$ if the transcript is active. In the inactive state initiation is not possible, while in the active state initiation is an exponential process with rate α. In practice, we add the reaction $\omega_k[0] = -2$ that corresponds to a change in transcript activity, $G \to \neg G$. The reaction time is drawn from an exponential distribution

$$\omega_k[1] \sim \begin{cases} \mathrm{Exp}(k_1) & \text{if } G = 0 \\ \mathrm{Exp}(k_0) & \text{if } G = 1. \end{cases}$$

We first simulate the model for 10^3 iterations of burn-in; for each trace we record the state of the system every $dt = 20$ s for a total duration of 90 min. The final state is used as a starting point to simulate the dynamics for 10^3 iterations before recording the following trace. For the run-off, we remove the initiation events possibly stored in Ω after the initial burn-in and before simulating the first trace with $\alpha = 0$. The last state of burn-in is then used as a starting point to simulate the dynamics for 10^3 more iterations before recording the following run-off.

To obtain the translation signal, we compute the number of epitopes $n(t)$ synthesized at each time point t by all the translating ribosomes. This is given by the scalar product

$$n(t) = \boldsymbol{w} \cdot \boldsymbol{\tau}(t) \tag{42}$$

where $\boldsymbol{w} \in \mathbb{N}^L$, with L the transcript size, containing the cumulative number of epitopes along the transcript, and $\boldsymbol{\tau} \in \{0, 1\}^L$ is the time-dependent occupation vector, with

$$\tau_i = \begin{cases} 0 & \text{if site } i \text{ is occupied} \\ 1 & \text{if site } i \text{ is free.} \end{cases} \tag{43}$$

The total intensity is given by $I_{\mathrm{S}}(t) = \frac{i_{\mathrm{MP}}}{24} n(t)$, where i_{MP} is the intensity of one mature protein and the suffix S stands for "simulated".

We add an offset b_0 to the intensity and we apply a log-normal noise to obtain the final simulated, noisy signal $y_{\mathrm{S}}(t)$:

$$P(y_{\mathrm{S}}(t) \mid \mu_{\mathrm{S}}(t), s_0) = \frac{1}{y_{\mathrm{S}}(t) s_0 \sqrt{2\pi}} \exp\left\{ -\frac{(\ln y_{\mathrm{S}}(t) - \ln \mu_{\mathrm{S}}(t))^2}{2 s_0^2} \right\} \tag{44}$$

where $\mu_{\mathrm{S}}(t) = b_0 + I_{\mathrm{S}}(t)$ and s_0 is the measurement noise, as described at the end of Bayesian modeling of run-off traces.

The duration of each trace is drawn from an exponential distribution with mean 10 min to mimic the tracking duration of one mRNA molecule in experiments. Simulated run-off traces are longer than 5 min (as in experiments, see Spot tracking and intensity quantification) and start at $t = 0$, when the run-off starts (approximately 60 s after HT addition, see Preprocessing and data filtering).

Data and code availability

Our computational models for analysis of SunTag traces are available on Github (https://github.com/naef-lab/suntag-analysis). SunTag run-off and steady-state raw images are available on Zenodo (https://doi.org/10.5281/zenodo.17669331).

Acknowledgments

We would like to thank the EPFL's Bioimaging and Optics Facility (BIOP) and Scientific IT & Application Support (SCITAS) for their assistance, as well as Eva Poch for her help with the Western blot experiments. We also appreciate the insightful discussions with Tobias Hochstoeger regarding the SunTag system. This research was supported by the Swiss National Science Foundation (SNSF) Sinergia grant #205884 to F.N. and J.C., the Swiss Cancer Research grant #KFS-5412-08-2021-R to F.N., and the École Polytechnique Fédérale de Lausanne.

Figures and Tables

Camera:	EMCCD Grayscale (ImagEMX2) 512 x 512 pixels, (16.0 x 16.5) µm/pixel 16-bit
Objective:	U PLAN S APO 60x 1.42NA
Laser lines:	488 nm 640 nm
Emission filters:	sdc GFP BP 525/50 (Chroma ET525/50m) sdc Cy5 BP 700/75 (Chroma ET700/75m)

Table 1. Technical specification of the live-cell imaging set-up.

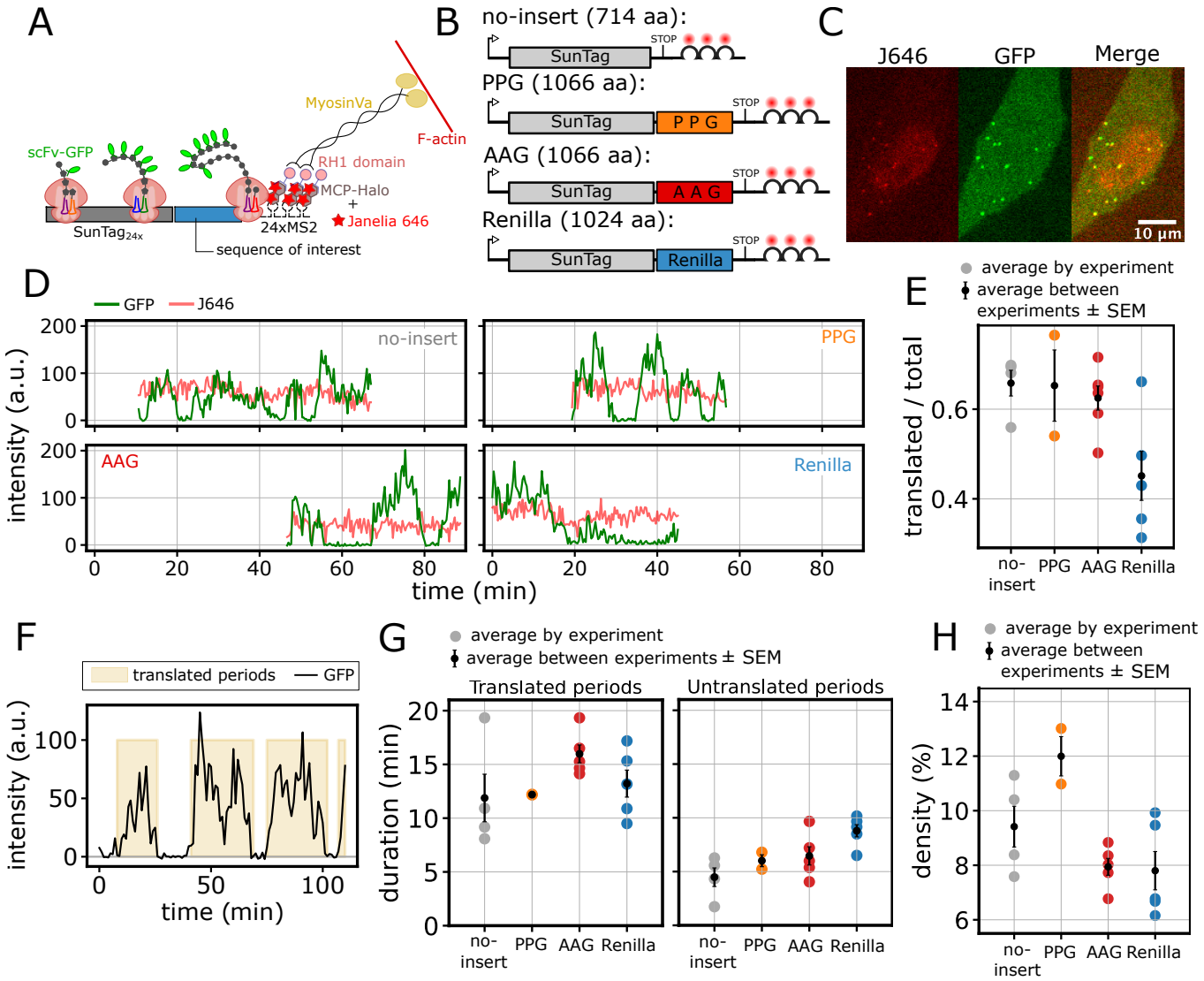

Figure 1. Translation exhibits bursts with low average ribosome density. (A) Schematic of the SunTag system used for single-molecule imaging of translation. **(B)** SunTag reporters differing in their coding sequence inserts: no insert, PPG (proline-rich), AAG (alanine-rich) and Renilla. **(C)** Representative live-cell image of a HeLa cell expressing the PPG reporter, showing JF646 (mRNA), GFP (nascent peptide), and merged signals. The image is part of a larger field of view, acquired with a 60X objective in a spinning-disk confocal setup. Scale bar, 10 µm. **(D)** Representative long traces for each reporter, showing stable JF646 (mRNA, red) and fluctuating GFP (SunTag, green) intensities over time. **(E)** Average fraction of translated traces for each reporter. Colored dots represent averages from individual experiments; black dots with bars show the mean ± SEM across multiple experiments (n traces, n experiments): no-insert (669, 4), PPG (440, 2), AAG (1235, 6), Renilla (804, 5). **(F)** Example of the SunTag signal of a translated mRNA (no-insert), highlighting translated periods (shaded yellow). **(G)** Average duration of translated periods (left) and untranslated periods (right) for traces longer than 20 min. Colored dots represent averages from individual experiments; black dots with bars show the mean ± SEM across multiple experiments (n traces, n experiments): no-insert (41, 4), PPG (45, 2), AAG (90, 5), Renilla (62, 5). **(H)** Estimated average ribosome density (percentage of transcript covered by ribosomes) for traces in (G). Significance tests performed with Mann-Whitney U test.

Figure 1—figure supplement 1. SunTag traces in control conditions.

Figure 1—figure supplement 2. Experimental measurement of mature protein intensities to estimate number of translating ribosomes.

Figure 1—video 1. Time-lapse imaging of HeLa cells expressing the AAG reporter.

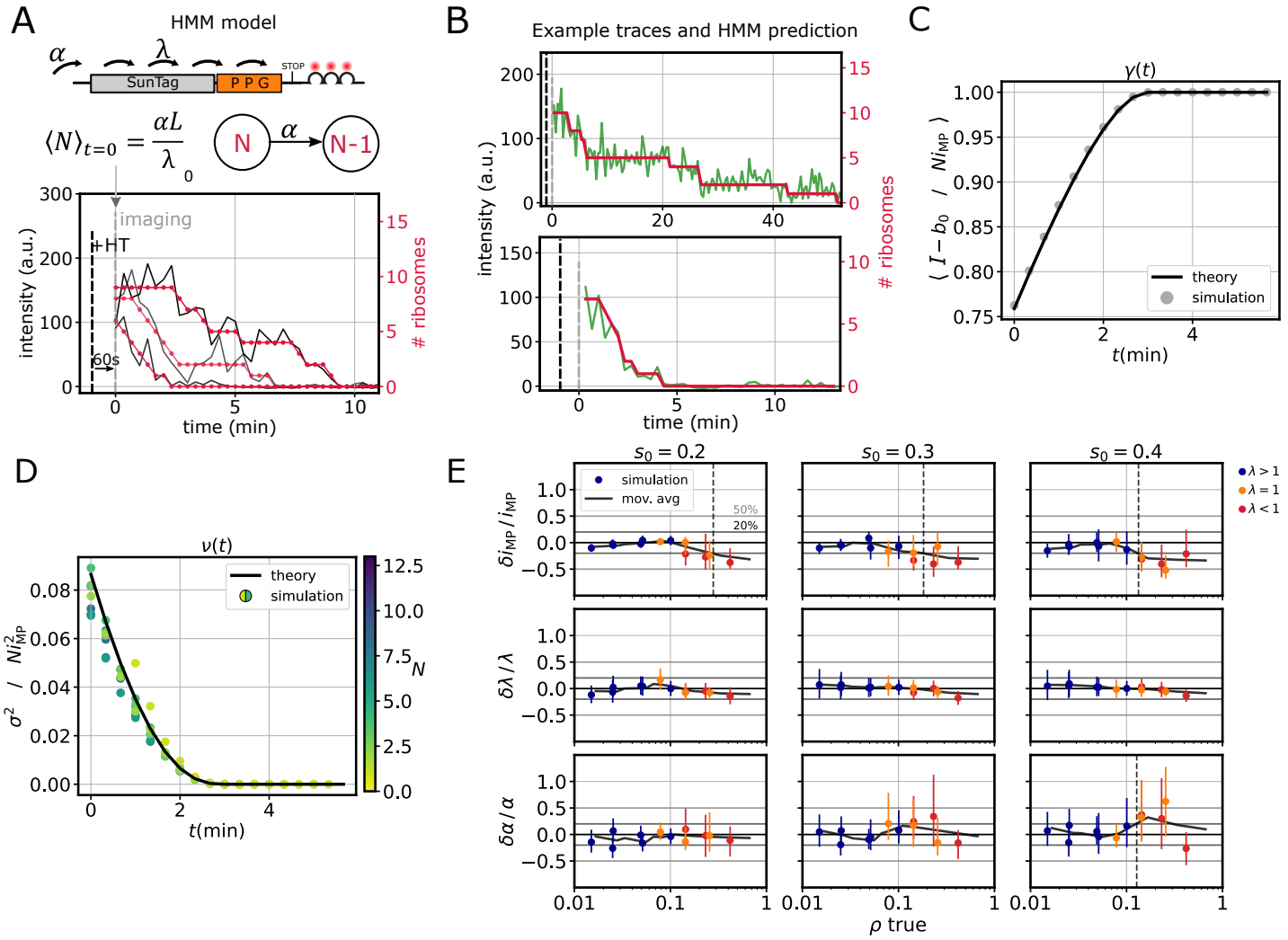

Figure 2. TASEP-based inference of translation dynamics from single run-off traces. (A) Schematic of the Hidden Markov Model (HMM) used to analyze run-off experiments. α = initiation rate, λ = average elongation rate, L = reporter length, $\langle N \rangle_{t=0}$ = average number of ribosomes at $t = 0$ (60 s after HT addition). **(B)** Representative slow (top) and fast (bottom) decaying traces from one run-off experiment with the PPG reporter; intensity in green and predicted number of ribosomes in red. **C)** Comparison between the analytical correction factor γ (black line, Methods ***Equation 24***) and the results obtained by numerical simulations of run-off traces (grey dots). The latter represent $(I(N,t) - b_0)/N i_{\mathrm{MP}}$ averaged over 2000 simulated run-off traces, with $I(N,t)$ simulated intensity, b_0 offset, N number of ribosomes and i_{MP} mature protein intensity. Kinetic parameters used in simulations: initiation $\alpha = 1/60\ \mathrm{s}^{-1}$, elongation $\lambda = 3.0\ \mathrm{aa/s}$. **D)** Comparison between the analytical correction factor ν (black line, Methods ***Equation 26***) and the results obtained by numerical simulations of run-off traces (coloured dots). The latter represent the normalized intensity variance $\sigma^2(N,t)/N i_{\mathrm{MP}}^2$ for different values of N, same simulated traces as in C). **E)** Relative error on model parameters (α, λ, i_{MP}) *vs* average ribosome density ρ, for different values of the noise parameter s_0 (Methods ***Equation 44***), for simulated run-off traces. Each data point is obtained with a different combination of $\lambda \in \{0.5, 1, 3, 5\}$ aa/s and $\alpha \in \{1/120, 1/60, 1/30\}\ \mathrm{s}^{-1}$. Blue dots represent the relative error on each parameter, the black curve is a moving average, and the dashed line indicates the density ρ at which the relative error goes beyond 0.2. Simulation parameters in C) – E): $i_{\mathrm{MP}} = 10$ a.u., reporter length $L = 1066$ aa, ribosome size $\ell = 10$ aa.

Figure 2—figure supplement 1. SunTag run-off traces in control conditions after HT addition.

Figure 2—figure supplement 2. TASEP-based inference accurately estimates ribosome density on simulated data despite correlations between α and i_{MP}.

Figure 2—video 1. Time-lapse imaging of HeLa cells expressing the PPG reporter after harringtonine treatment.

Figure 2—video 2. Time-lapse imaging of HeLa cells expressing the AAG reporter after harringtonine treatment.

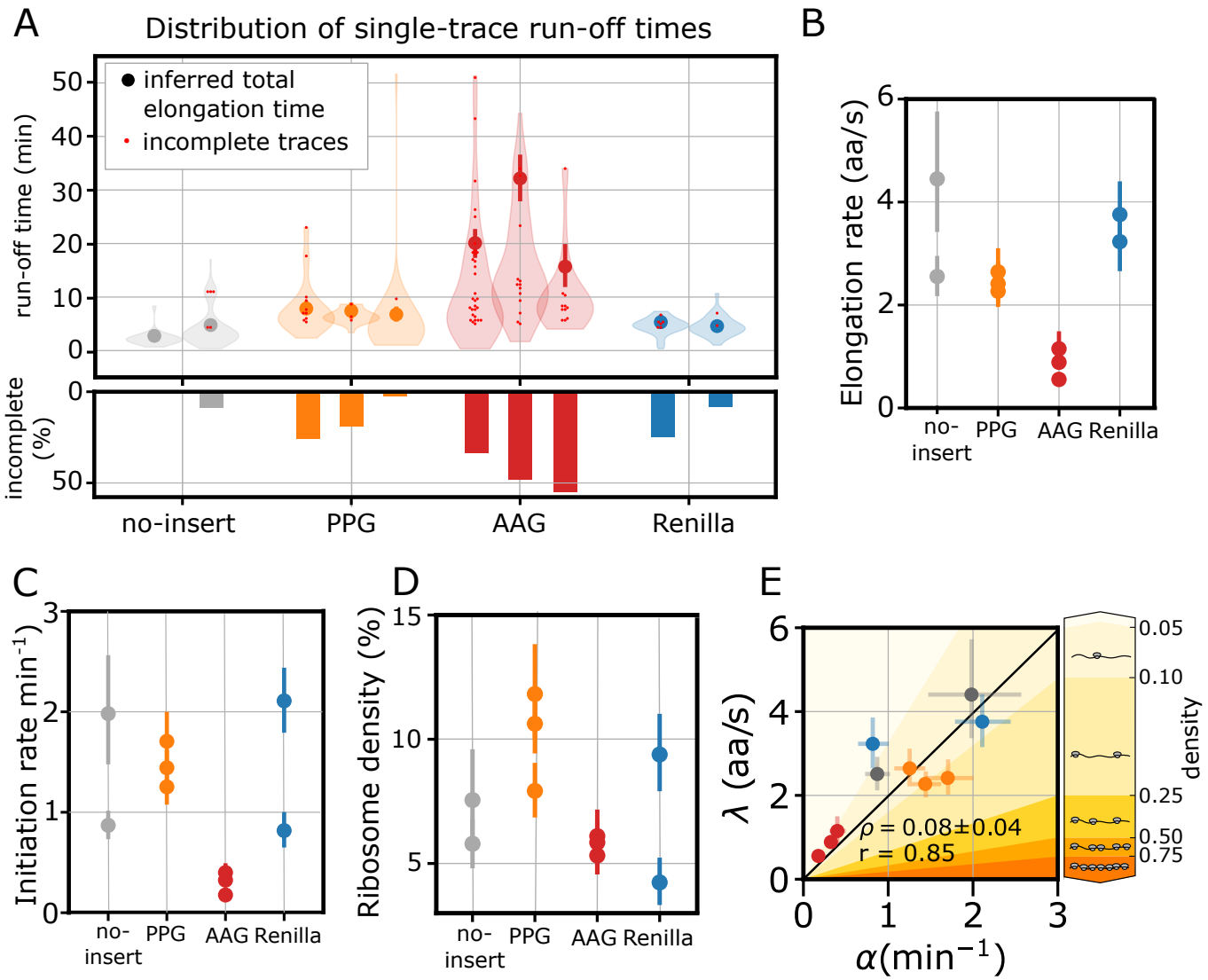

Figure 3. Low ribosome density arises from coordinated translation initiation and elongation. In all panels the error bars indicate 95% confidence intervals. **(A)** Run-off time distribution (top) and percentage of incomplete run-offs (bottom) for each reporter. For incomplete runoffs we include the total duration of the trace, as it represents a lower-bound to the total run-off time (red dots). **(B)** Inferred elongation rates (λ). **(C)** Inferred initiation rates (α). **(D)** Inferred average ribosome density. **(E)** Correlation between elongation and initiation rates for each experiment. The shaded background indicates approximate ribosome density regimes, ranging from low density (light yellow) to high density (dark yellow), as shown by the adjacent color bar. ρ indicates the average density ± standard deviation, r is the Pearson correlation coefficient.

Figure 3—figure supplement 1. Global measurement noise estimation from CHX traces.

Figure 3—figure supplement 2. HMM approach predicts lower elongation speed than simple linear regression and suggests the presence of bursting and stalling.

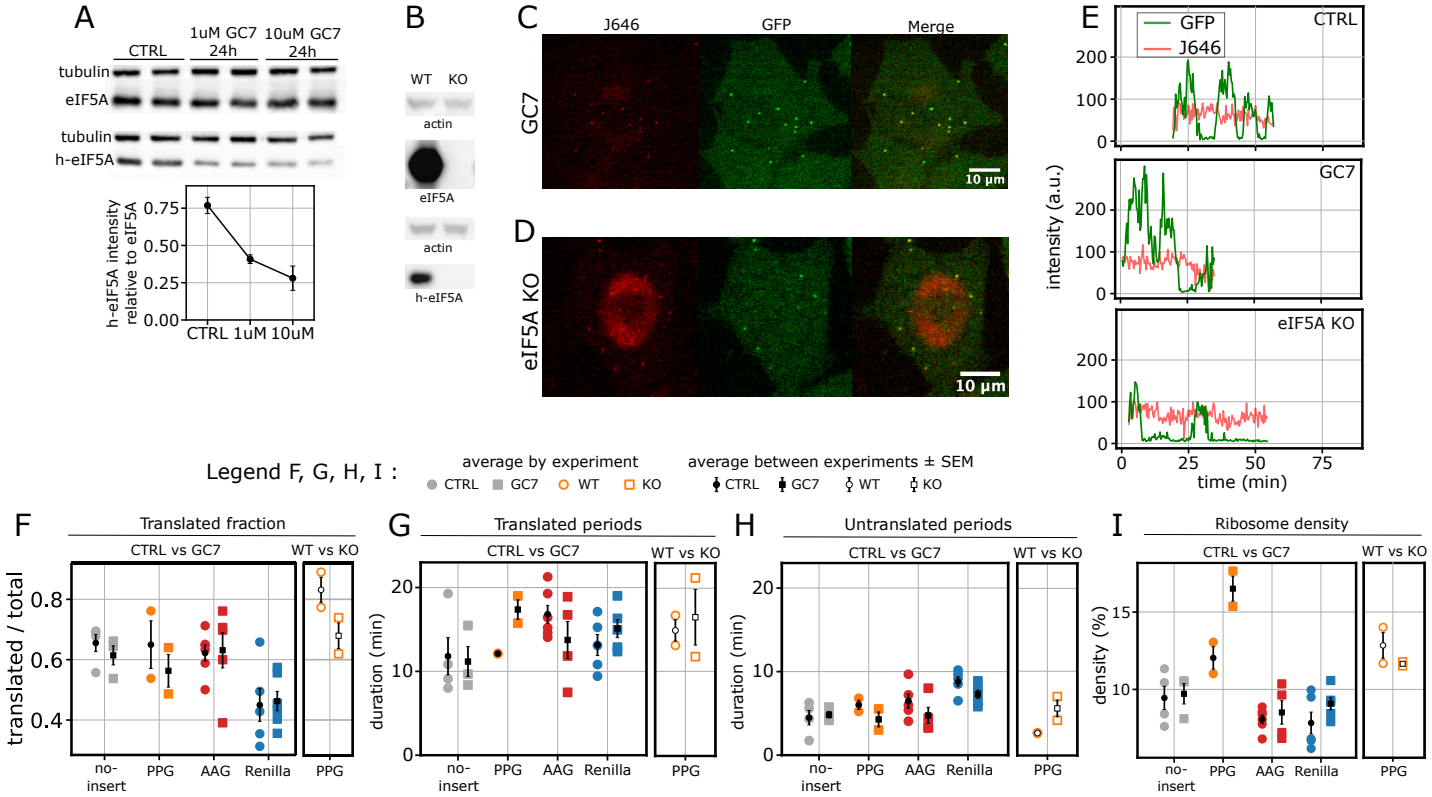

Figure 4. eIF5A perturbations minimally affects ribosome density and translational bursting. (A) Top: western blot of h-eIF5A levels in control cells and cells treated with 1 µM and 10 µM GC7 for 24 hours, with 1 mM AG. Bottom: quantification of h-eIF5A signal relative to total eIF5A. Error bars represent standard deviation between replicates. **(B)** Total eIF5A and h-eIF5A expression in CRISPR/Cas9 knock-out (KO) clones compared to wild-type (WT) HeLa cells. **(C)** Representative live-cell images of a HeLa cell expressing the PPG reporter after 24-hour treatment with 1 µM GC7 and 1 mM AG, showing JF646 (mRNA, red), GFP (SunTag, green), and merged signals. The image is part of a larger field of view, acquired with a 60X objective in a spinning-disk confocal set-up. Scale bar, 10 µm. **(D)** Same as (C) for eIF5A KO cells. **(E)** Representative traces of the PPG reporter under control conditions, GC7 treatment, and eIF5A KO, showing GFP (SunTag, green) and J646 (mRNA, red) intensities over time. **(F)** Fraction of translated mRNAs (n traces, n experiments): no-insert CTRL (669, 4), GC7 (511, 3); PPG CTRL (440, 2), GC7 (392, 2); AAG CTRL (1235, 6), GC7 (900, 5); Renilla CTRL (804, 5), GC7 (1476, 6); PPG WT (396, 2), KO (343, 2). **(G)** Average duration of translated periods and **(H)** untranslated periods for traces longer than 20 min. **(I)** Average ribosome density during the translated periods analyzed in (G). **(G – I)** (n traces > 20 min, n experiments): no-insert CTRL (41, 4), GC7 (20, 3); PPG CTRL (45, 2), GC7 (28, 2); AAG CTRL (90, 5), GC7 (26, 4); Renilla CTRL (62, 5), GC7 (112, 5); PPG WT (33, 2), KO (26, 2). Colored dots represent averages from individual experiments, black dots with bars show the mean ± SEM across multiple experiments. Mann-Whitney U significance test.

Figure 4—figure supplement 1. SunTag traces in perturbed conditions.

Figure 4—video 1. Time-lapse imaging of HeLa cells expressing the PPG reporter after 24h GC7 treatment.

Figure 4—video 2. Time-lapse imaging of EIF5A KO HeLa cells expressing the PPG reporter.

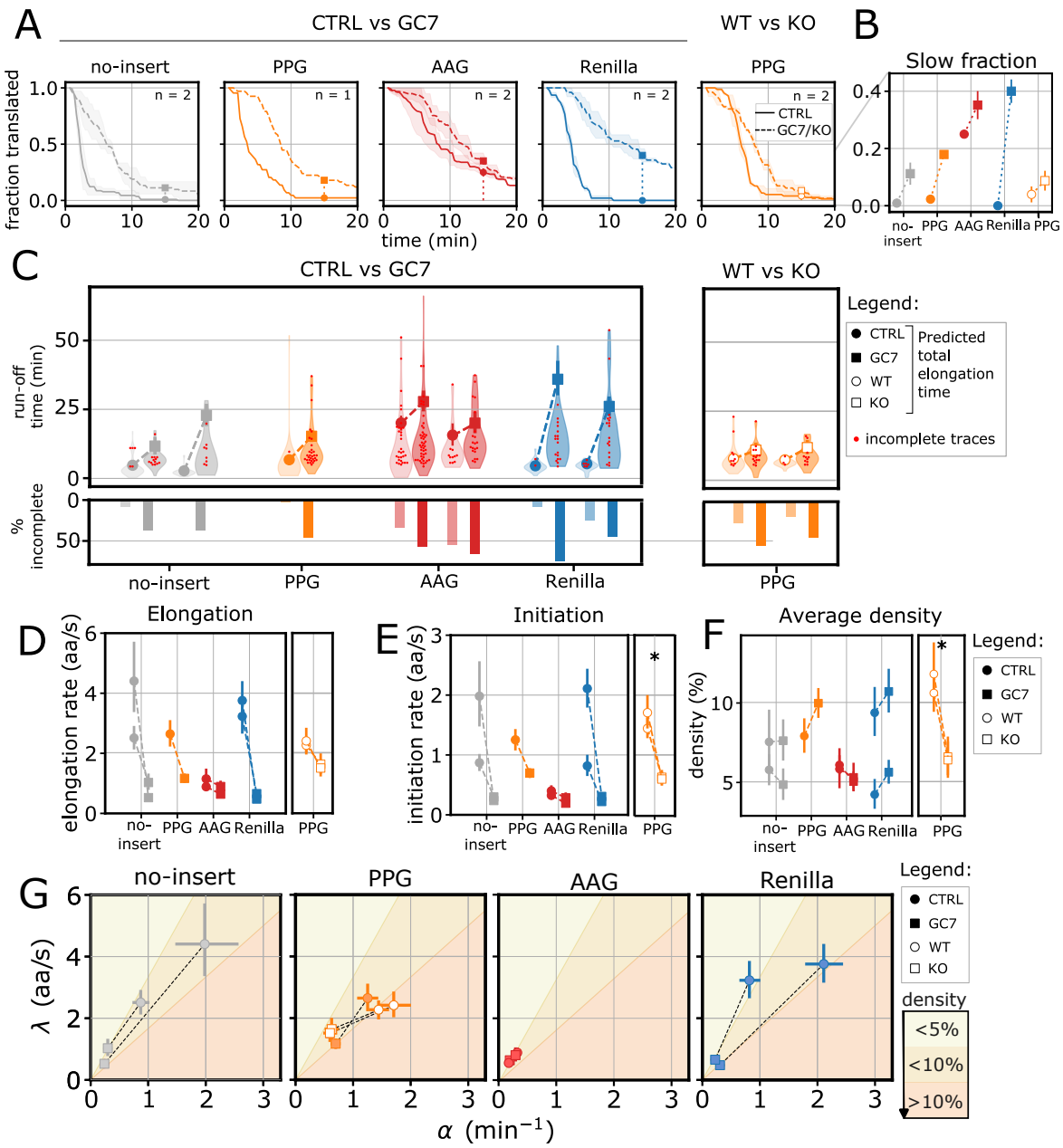

Figure 5. eIF5A-driven elongation changes induce initiation regulation to preserve ribosome density. (A) Fraction of translated mRNAs over time in control (solid lines) and perturbed conditions (GC7 treatment and eIF5A KO, dashed lines) for each reporter. Thick lines represent the mean across experiments, shaded areas represent standard deviation between experiments. Full circles and squares represent the fraction of mRNAs still translated 15 min after HT addition (control and perturbed conditions, respectively). (n is the number of experiments) **(B)** Fraction of translated traces showing slow run-off (still translated after 15 min of HT treatment). **(C)** Run-off time distribution (top) and percentage of incomplete run-offs (bottom) for each reporter in control conditions (circles) and perturbed conditions (GC7 treatment and eIF5A KO, squares). For incomplete runoffs we include the total duration of the trace, as it represents a lower-bound to the total run-off time (red dots). Number of translated traces (control, perturbed): no-insert (58, 35), (22, 24); PPG (45, 67); AAG (93, 80), (20, 32); Renilla (24, 24), (24, 40); PPG WT/KO (39, 28), (16, 25). **(D)** Inferred elongation rates. **(E)** Inferred initiation rates. **(F)** Inferred average ribosome density. **(G)** Representation of changes in translation kinetic parameters upon eIF5A perturbation in the initiation-elongation ($\alpha - \lambda$) plane. The shaded background indicates approximate ribosome density regimes, ranging from low density (light yellow) to high density (dark yellow), as shown by the adjacent color bar. Significance tests performed with Mann-Whitney U test.

Figure 5—figure supplement 1. SunTag run-off traces in perturbed conditions after HT addition.

Figure 5—figure supplement 2. Inferred mature protein intensities are in good agreement with the experimental measurement.

Figure 5—video 1. Time-lapse imaging of HeLa cells expressing the PPG reporter after 24h GC7 treatment and harringtonine addition.

Figure 5—video 2. Time-lapse imaging of HeLa cells expressing the AAG reporter after after 24h GC7 treatment and harringtonine addition.

Figure 5—video 3. Time-lapse imaging of EIF5A KO HeLa cells expressing the PPG reporter after harringtonine addition.

References

Absmeier E, Chandrasekaran V, O'Reilly FJ, Stowell JA, Rappsilber J, Passmore LA. Specific recognition and ubiquitination of slow-moving ribosomes by human CCR4-NOT. bioRxiv. 2022 Jul; http://dx.doi.org/10.1101/2022.07.24.501325, doi: 10.1101/2022.07.24.501325.

Aguilera LU, Raymond W, Fox ZR, May M, Djokic E, Morisaki T, Stasevich TJ, Munsky B. Computational design and interpretation of single-RNA translation experiments. PLOS Computational Biology. 2019 Oct; 15(10):e1007425. https://journals.plos.org/ploscompbiol/article?id=10.1371/journal.pcbi.1007425, doi: 10.1371/journal.pcbi.1007425, publisher: Public Library of Science.

Amaya Ramirez CC, Hubbe P, Mandel N, Béthune J. 4EHP-independent repression of endogenous mRNAs by the RNA-binding protein GIGYF2. Nucleic Acids Research. 2018 Mar; 46(11):5792–5808. http://dx.doi.org/10.1093/nar/gky198, doi: 10.1093/nar/gky198.

Andreev DE, Arnold M, Kiniry SJ, Loughran G, Michel AM, Rachinskii D, Baranov PV. TASEP modelling provides a parsimonious explanation for the ability of a single uorf to derepress translation during the integrated stress response. eLife. 2018 Jun; 7. doi: 10.7554/eLife.32563, publisher: eLife Sciences Publications Ltd.

Bae H, Coller J. Codon optimality-mediated mRNA degradation: Linking translational elongation to mRNA stability. Molecular Cell. 2022 Apr; 82(8):1467–1476. http://dx.doi.org/10.1016/j.molcel.2022.03.032, doi: 10.1016/j.molcel.2022.03.032.

Banaszynski LA, Chen Lc, Maynard-Smith LA, Ooi AGL, Wandless TJ. A Rapid, Reversible, and Tunable Method to Regulate Protein Function in Living Cells Using Synthetic Small Molecules. Cell. 2006 Sep; 126(5):995–1004. http://dx.doi.org/10.1016/j.cell.2006.07.025, doi: 10.1016/j.cell.2006.07.025.

Barba-Aliaga M, Mena A, Espinoza V, Apostolova N, Costell M, Alepuz P. Hypusinated eIF5A is required for the translation of collagen. Journal of Cell Science. 2021 Sep; 134(18). http://dx.doi.org/10.1242/jcs.258643, doi: 10.1242/jcs.258643.

Barrington CL, Galindo G, Koch AL, Horton ER, Morrison EJ, Tisa S, Stasevich TJ, Rissland OS. Synonymous codon usage regulates translation initiation. Cell Reports. 2023 Dec; 42(12):113413. http://dx.doi.org/10.1016/j.celrep.2023.113413, doi: 10.1016/j.celrep.2023.113413.

Bazzini AA, Viso F, Moreno-Mateos MA, Johnstone TG, Vejnar CE, Qin Y, Yao J, Khokha MK, Giraldez AJ. Codon identity regulates mRNA stability and translation efficiency during the maternal-to-zygotic transition. The EMBO Journal. 2016; 35(19):2087–2103. doi: 10.15252/embj.201694699.

Betancourt MJ, Girolami M. Hamiltonian Monte Carlo for Hierarchical Models. arXiv. 2013; https://arxiv.org/abs/1312.0906, doi: 10.48550/ARXIV.1312.0906.

Bhaskar V, Jia M, Chao JA. In: A Single-Molecule RNA Mobility Assay to Identify Proteins that Link RNAs to Molecular Motors Springer US; 2020. p. 269–282. http://dx.doi.org/10.1007/978-1-0716-0712-1_16, doi: 10.1007/978-1-0716-0712-1_16.

Bicknell AA, Reid DW, Licata MC, Jones AK, Cheng YM, Li M, Hsiao CJ, Pepin CS, Metkar M, Levdansky Y, Fritz BR, Andrianova EA, Jain R, Valkov E, Köhrer C, Moore MJ. Attenuating ribosome load improves protein output from mRNA by limiting translation-dependent mRNA decay. Cell Reports. 2024 Apr; 43(4):114098. http://dx.doi.org/10.1016/j.celrep.2024.114098, doi: 10.1016/j.celrep.2024.114098.

Boersma S, Khuperkar D, Verhagen BMP, Sonneveld S, Grimm JB, Lavis LD, Tanenbaum ME. Multi-Color Single-Molecule Imaging Uncovers Extensive Heterogeneity in mRNA Decoding. Cell. 2019 Jul; 178(2):458–472.e19. https://linkinghub.elsevier.com/retrieve/pii/S0092867419304994, doi: 10.1016/j.cell.2019.05.001.

Buschauer R, Matsuo Y, Sugiyama T, Chen YH, Alhusaini N, Sweet T, Ikeuchi K, Cheng J, Matsuki Y, Nobuta R, Gilmozzi A, Berninghausen O, Tesina P, Becker T, Coller J, Inada T, Beckmann R. The Ccr4-Not complex monitors the translating ribosome for codon optimality. Science. 2020 Apr; 368(6488). http://dx.doi.org/10.1126/science.aay6912, doi: 10.1126/science.aay6912.

Choi H, Liao YC, Yoon YJ, Grimm J, Wang N, Lavis LD, Singer RH, Lippincott-Schwartz J. Secretome translation shaped by lysosomes and lunapark-marked ER junctions. Nature. 2025 Nov; http://dx.doi.org/10.1038/s41586-025-09718-0, doi: 10.1038/s41586-025-09718-0.

Coni S, Serrao SM, Yurtsever ZN, Di Magno L, Bordone R, Bertani C, Licursi V, Ianniello Z, Infante P, Moretti M, Petroni M, Guerrieri F, Fatica A, Macone A, De Smaele E, Di Marcotullio L, Giannini G, Maroder M, Agostinelli E, Canettieri G. Blockade of EIF5A hypusination limits colorectal cancer growth by inhibiting MYC elongation. Cell Death & Disease. 2020 Dec; 11(12). http://dx.doi.org/10.1038/s41419-020-03174-6, doi: 10.1038/s41419-020-03174-6.

Dufourt J, Bellec M, Trullo A, Dejean M, De Rossi S, Favard C, Lagha M. Imaging translation dynamics in live embryos reveals spatial heterogeneities. Science. 2021 May; 372(6544):840–844. http://dx.doi.org/10.1126/science.abc3483, doi: 10.1126/science.abc3483.

Erdmann-Pham DD, Dao Duc K, Song YS. The Key Parameters that Govern Translation Efficiency. Cell Systems. 2020; 10(2):183–192.e6. https://doi.org/10.1016/j.cels.2019.12.003, doi: 10.1016/j.cels.2019.12.003, publisher: Elsevier Inc. _eprint: 1803.05609.

Ershov D, Phan MS, Pylvänäinen JW, Rigaud SU, Le Blanc L, Charles-Orszag A, Conway JRW, Laine RF, Roy NH, Bonazzi D, Duménil G, Jacquemet G, Tinevez JY. TrackMate 7: integrating state-of-the-art segmentation algorithms into tracking pipelines. Nature Methods. 2022 Jun; 19(7):829–832. http://dx.doi.org/10.1038/s41592-022-01507-1, doi: 10.1038/s41592-022-01507-1.

Fresno M, Jiménez A, Vásquez D. Inhibition of Translation in Eukaryotic Systems by Harringtonine. European Journal of Biochemistry. 1977 Jan; 72(2):323–330. http://dx.doi.org/10.1111/j.1432-1033.1977.tb11256.x, doi: 10.1111/j.1432-1033.1977.tb11256.x.

Gillespie DT. A general method for numerically simulating the stochastic time evolution of coupled chemical reactions. Journal of Computational Physics. 1976; doi: 10.1016/0021-9991(76)90041-3.

Giraud S, Kerforne T, Zely J, Ameteau V, Couturier P, Tauc M, Hauet T. The inhibition of eIF5A hypusination by GC7, a preconditioning protocol to prevent brain death-induced renal injuries in a preclinical porcine kidney transplantation model. American Journal of Transplantation. 2020 Dec; 20(12):3326–3340. http://dx.doi.org/10.1111/ajt.15994, doi: 10.1111/ajt.15994.

Gobet C, Weger BD, Marquis J, Martin E, Neelagandan N, Gachon F, Naef F. Robust landscapes of ribosome dwell times and aminoacyl-tRNAs in response to nutrient stress in liver. Proceedings of the National Academy of Sciences. 2020 Apr; p. 201918145. http://www.pnas.org/lookup/doi/10.1073/pnas.1918145117, doi: 10.1073/pnas.1918145117, publisher: National Academy of Sciences.

Goldman DH, Livingston NM, Movsik J, Wu B, Green R. Live-cell imaging reveals kinetic determinants of quality control triggered by ribosome stalling. Molecular Cell. 2021 Apr; 81(8):1830–1840.e8. https://linkinghub.elsevier.com/retrieve/pii/S1097276521000496, doi: 10.1016/j.molcel.2021.01.029.

Gutierrez E, Shin BS, Woolstenhulme CJ, Kim JR, Saini P, Buskirk AR, Dever TE. eIF5A Promotes Translation of Polyproline Motifs. Molecular Cell. 2013 Jul; 51(1):35–45. https://linkinghub.elsevier.com/retrieve/pii/S1097276513003262, doi: 10.1016/j.molcel.2013.04.021.

Hickey KL, Dickson K, Cogan JZ, Replogle JM, Schoof M, D'Orazio KN, Sinha NK, Hussmann JA, Jost M, Frost A, Green R, Weissman JS, Kostova KK. GIGYF2 and 4EHP Inhibit Translation Initiation of Defective Messenger RNAs to Assist Ribosome-Associated Quality Control. Molecular Cell. 2020 Sep; 79(6):950–962.e6. https://linkinghub.elsevier.com/retrieve/pii/S1097276520304731, doi: 10.1016/j.molcel.2020.07.007.

Hinnebusch AG, Ivanov IP, Sonenberg N. Translational control by 5'-untranslated regions of eukaryotic mRNAs. Science. 2016 Jun; 352(6292):1413–1416. http://dx.doi.org/10.1126/science.aad9868, doi: 10.1126/science.aad9868.

Huter P, Arenz S, Bock LV, Graf M, Frister JO, Heuer A, Peil L, Starosta AL, Wohlgemuth I, Peske F, Nováček J, Berninghausen O, Grubmüller H, Tenson T, Beckmann R, Rodnina MV, Vaiana AC, Wilson DN. Structural Basis for Polyproline-Mediated Ribosome Stalling and Rescue by the Translation Elongation Factor EF-P. Molecular Cell. 2017 Nov; 68(3):515–527.e6. https://linkinghub.elsevier.com/retrieve/pii/S109727651730789X, doi: 10.1016/j.molcel.2017.10.014.

Ingolia NT, Ghaemmaghami S, Newman JRS, Weissman JS. Genome-wide analysis in vivo of translation with nucleotide resolution using ribosome profiling. Science. 2009; 324(5924):218–223. doi: 10.1126/science.1168978.

Ingolia NT, Lareau LF, Weissman JS. Ribosome Profiling of Mouse Embryonic Stem Cells Reveals the Complexity and Dynamics of Mammalian Proteomes. Cell. 2011 Nov; 147(4):789–802. https://linkinghub.elsevier.com/retrieve/pii/S0092867411011925, doi: 10.1016/j.cell.2011.10.002.

Joazeiro CAP. Mechanisms and functions of ribosome-associated protein quality control. Nature Reviews Molecular Cell Biology. 2019; 20(6):368–383. http://dx.doi.org/10.1038/s41580-019-0118-2, doi: 10.1038/s41580-019-0118-2, publisher: Springer US.

Juszkiewicz S, Slodkowicz G, Lin Z, Freire-Pritchett P, Peak-Chew SY, Hegde RS. Ribosome collisions trigger cis-acting feedback inhibition of translation initiation. eLife. 2020 Jul; 9:e60038. https://elifesciences.org/articles/60038, doi: 10.7554/eLife.60038.

Komar AA, Samatova E, Rodnina MV. Translation Rates and Protein Folding. Journal of Molecular Biology. 2024 Jul; 436(14):168384. http://dx.doi.org/10.1016/j.jmb.2023.168384, doi: 10.1016/j.jmb.2023.168384.

Lassak J, Wilson DN, Jung K. Stall no more at polyproline stretches with the translation elongation factors EF-P and IF-5A. Molecular Microbiology. 2015 Nov; 99(2):219–235. http://dx.doi.org/10.1111/mmi.13233, doi: 10.1111/mmi.13233.

Latallo MJ, Wang S, Dong D, Nelson B, Livingston NM, Wu R, Zhao N, Stasevich TJ, Bassik MC, Sun S, Wu B. Single-molecule imaging reveals distinct elongation and frameshifting dynamics between frames of expanded RNA repeats in C9ORF72-ALS/FTD. Nature Communications. 2023 Sep; 14(1). http://dx.doi.org/10.1038/s41467-023-41339-x, doi: 10.1038/s41467-023-41339-x.

Levin D, Tuller T. Genome-Scale Analysis of Perturbations in Translation Elongation Based on a Computational Model. Scientific Reports. 2018 Nov; 8(1):16191. https://www.nature.com/articles/s41598-018-34496-3, doi: 10.1038/s41598-018-34496-3, number: 1 Publisher: Nature Publishing Group.

Li S, Ikeuchi K, Kato M, Buschauer R, Sugiyama T, Adachi S, Kusano H, Natsume T, Berninghausen O, Matsuo Y, Becker T, Beckmann R, Inada T. Sensing of individual stalled 80S ribosomes by Fap1 for nonfunctional rRNA turnover. Molecular Cell. 2022 Sep; 82(18):3424–3437.e8. http://dx.doi.org/10.1016/j.molcel.2022.08.018, doi: 10.1016/j.molcel.2022.08.018.

Livingston NM, Kwon J, Valera O, Saba JA, Sinha NK, Reddy P, Nelson B, Wolfe C, Ha T, Green R, Liu J, Wu B. Bursting translation on single mRNAs in live cells. Molecular Cell. 2023; doi: 10.1016/j.molcel.2023.05.019.

Lyons EF, Devanneaux LC, Muller RY, Freitas AV, Meacham ZA, McSharry MV, Trinh VN, Rogers AJ, Ingolia NT, Lareau LF. Translation elongation as a rate limiting step of protein production. bioRxiv. 2023 Nov; http://dx.doi.org/10.1101/2023.11.27.568910, doi: 10.1101/2023.11.27.568910.

Madern MF, Yang S, Witteveen O, Segeren HA, Bauer M, Tanenbaum ME. Long-term imaging of individual ribosomes reveals ribosome cooperativity in mRNA translation. Cell. 2025 Jan; http://dx.doi.org/10.1016/j.cell.2025.01.016, doi: 10.1016/j.cell.2025.01.016.

Maier B, Ogihara T, Trace AP, Tersey SA, Robbins RD, Chakrabarti SK, Nunemaker CS, Stull ND, Taylor CA, Thompson JE, Dondero RS, Lewis EC, Dinarello CA, Nadler JL, Mirmira RG. The unique hypusine modification of eIF5A promotes islet β cell inflammation and dysfunction in mice. Journal of Clinical Investigation. 2010 Jun; 120(6):2156–2170. http://dx.doi.org/10.1172/JCI38924, doi: 10.1172/jci38924.

Mandal A, Mandal S, Park MH. Global quantitative proteomics reveal up-regulation of endoplasmic reticulum stress response proteins upon depletion of eIF5A in HeLa cells. Scientific Reports. 2016 May; 6(1). http://dx.doi.org/10.1038/srep25795, doi: 10.1038/srep25795.

Manjunath H, Zhang H, Rehfeld F, Han J, Chang TC, Mendell JT. Suppression of Ribosomal Pausing by eIF5A Is Necessary to Maintain the Fidelity of Start Codon Selection. Cell Reports. 2019 Dec; 29(10):3134–3146.e6. https://linkinghub.elsevier.com/retrieve/pii/S2211124719314627, doi: 10.1016/j.celrep.2019.10.129.

Mateju D, Eichenberger B, Voigt F, Eglinger J, Roth G, Chao JA. Single-Molecule Imaging Reveals Translation of mRNAs Localized to Stress Granules. Cell. 2020; 183(7):1801–1812.e13. https://www.sciencedirect.com/science/article/pii/S0092867420315270, doi: https://doi.org/10.1016/j.cell.2020.11.010.

Matsumoto K, Kurokawa R, Takase M, Schneider-Poetsch T, Ling F, Suzuki T, Han P, Wakigawa T, Suzuki M, Tariq M, Ito A, Higashi K, Iwasaki S, Dohmae N, Yoshida M. Chemical genetic interaction linking eIF5A hypusination and mitochondrial integrity. Cold Spring Harbor Laboratory. 2023 Dec; http://dx.doi.org/10.1101/2023.12.20.571781, doi: 10.1101/2023.12.20.571781.

Mayr C. What Are 3′ UTRs Doing? Cold Spring Harbor Perspectives in Biology. 2018 Sep; 11(10):a034728. http://dx.doi.org/10.1101/cshperspect.a034728, doi: 10.1101/cshperspect.a034728.

Morisaki T, Stasevich TJ. Quantifying Single mRNA Translation Kinetics in Living Cells. Cold Spring Harbor Perspectives in Biology. 2018; 10(11). doi: 10.1101/cshperspect.a032078.

Narula A, Ellis J, Taliaferro JM, Rissland OS. Coding regions affect mRNA stability in human cells. RNA. 2019 Dec; 25(12):1751–1764. http://rnajournal.cshlp.org/lookup/doi/10.1261/rna.073239.119, doi: 10.1261/rna.073239.119.

Neelagandan N, Lamberti I, Carvalho HJF, Gobet C, Naef F. What determines eukaryotic translation elongation: recent molecular and quantitative analyses of protein synthesis. Open Biology. 2020 Dec; 10(12). http://dx.doi.org/10.1098/rsob.200292, doi: 10.1098/rsob.200292.

Pelechano V, Alepuz P. EIF5A facilitates translation termination globally and promotes the elongation of many non polyproline-specific tripeptide sequences. Nucleic Acids Research. 2017; 45(12):7326–7338. doi: 10.1093/nar/gkx479.

Plotkin JB, Kudla G. Synonymous but not the same: the causes and consequences of codon bias. Nature Reviews Genetics. 2011 Jan; 12(1):32–42. http://www.nature.com/articles/nrg2899, doi: 10.1038/nrg2899.

Presnyak V, Alhusaini N, Chen YH, Martin S, Morris N, Kline N, Olson S, Weinberg D, Baker KE, Graveley BR, Coller J. Codon optimality is a major determinant of mRNA stability. Cell. 2015; 160(6):1111–1124. http://dx.doi.org/10.1016/j.cell.2015.02.029, doi: 10.1016/j.cell.2015.02.029, publisher: Elsevier Inc.

Riba A, Nanni ND, Mittal N, Arhné E, Schmidt A, Zavolan M. Protein synthesis rates and ribosome occupancies reveal determinants of translation elongation rates. Proceedings of the National Academy of Sciences of the United States of America. 2019; 116(30):15023–15032. doi: 10.1073/pnas.1817299116.

Rossi D, Galvão FC, Bellato HM, Boldrin PEG, Andrews BJ, Valentini SR, Zanelli CF. eIF5A has a function in the cotranslational translocation of proteins into the ER. Amino Acids. 2013 Dec; 46(3):645–653. http://dx.doi.org/10.1007/s00726-013-1618-6, doi: 10.1007/s00726-013-1618-6.

Schuller AP, Wu CCC, Dever TE, Buskirk AR, Green R. eIF5A Functions Globally in Translation Elongation and Termination. Molecular Cell. 2017 Apr; 66(2):194–205.e5. https://linkinghub.elsevier.com/retrieve/pii/S1097276517301703, doi: 10.1016/j.molcel.2017.03.003.

Schultz CR, Geerts D, Mooney M, El-Khawaja R, Koster J, Bachmann AS. Synergistic drug combination GC7/DFMO suppresses hypusine/spermidine-dependent eIF5A activation and induces apoptotic cell death in neuroblastoma. Biochemical Journal. 2018 Jan; 475(2):531–545. http://dx.doi.org/10.1042/BCJ20170597, doi: 10.1042/bcj20170597.

Shah P, Ding Y, Niemczyk M, Kudla G, Plotkin JB. Rate-Limiting Steps in Yeast Protein Translation. Cell. 2013; http://dx.doi.org/10.1016/j.cell.2013.05.049, doi: 10.1016/j.cell.2013.05.049.

Sharma AK, Sormanni P, Ahmed N, Ciryam P, Friedrich UA, Kramer G, O'Brien EP. A chemical kinetic basis for measuring translation initiation and elongation rates from ribosome profiling data. PLoS Computational Biology. 2019; 15(5):1–27. doi: 10.1371/journal.pcbi.1007070, iSBN: 1111111111.

Shoulders MD, Raines RT. Collagen Structure and Stability. Annual Review of Biochemistry. 2009 Jun; 78(1):929–958. http://dx.doi.org/10.1146/annurev.biochem.77.032207.120833, doi: 10.1146/annurev.biochem.77.032207.120833.

Szavits-Nossan J, Grima R. Uncovering the effect of RNA polymerase steric interactions on gene expression noise: analytical distributions of nascent and mature RNA numbers. arXiv. 2023; http://arxiv.org/abs/2304.05304.

Szavits-Nossan J, Ciandrini L. Accurate measures of translation efficiency and traffic using ribosome profiling. bioRxiv. 2019 Apr; p. 719302. doi: 10.1101/719302, publisher: Cold Spring Harbor Laboratory.

Szavits-Nossan J, Romano MC, Ciandrini L. Power series solution of the inhomogeneous exclusion process. Phys Rev E. 2018 May; 97:052139. https://link.aps.org/doi/10.1103/PhysRevE.97.052139, doi: 10.1103/PhysRevE.97.052139.

Szepesi A, Kakas E, Szőllősi R, Molnár A, Pálfi P. Application of GC7 to reduce hypusination via inhibiting deoxyhypusine synthase in Arabidopsis thaliana seedlings exposed salt stress. Plant Stress. 2023 Dec; 10:100257. http://dx.doi.org/10.1016/j.stress.2023.100257, doi: 10.1016/j.stress.2023.100257.

Tanenbaum ME, Gilbert LA, Qi LS, Weissman JS, Vale RD. A Protein-Tagging System for Signal Amplification in Gene Expression and Fluorescence Imaging. Cell. 2014 Oct; 159(3):635–646. https://www.cell.com/cell/abstract/S0092-8674(14)01227-6, doi: 10.1016/j.cell.2014.09.039, publisher: Elsevier.

Team SD. Stan Modeling Language Users Guide and Reference Manual, v 2.34. . 2024; https://mc-stan.org.

Voigt F, Zhang H, Cui XA, Triebold D, Liu AX, Eglinger J, Lee ES, Chao JA, Palazzo AF. Single-Molecule Quantification of Translation-Dependent Association of mRNAs with the Endoplasmic Reticulum. Cell Reports. 2017; 21(13):3740–3753. https://www.sciencedirect.com/science/article/pii/S2211124717318041, doi: https://doi.org/10.1016/j.celrep.2017.12.008.

Wang C, Han B, Zhou R, Zhuang X. Real-Time Imaging of Translation on Single mRNA Transcripts in Live Cells. Cell. 2016; 165(4):990–1001. https://www.sciencedirect.com/science/article/pii/S0092867416304834, doi: https://doi.org/10.1016/j.cell.2016.04.040.

Weidenfeld I, Gossen M, Löw R, David Kentner D, Berger S, Görlich D, Bartsch D, Bujard H, Schönig K. Inducible expression of coding and inhibitory RNAs from retargetable genomic loci. Nucleic Acids Research. 2009; doi: 10.1093/nar/gkp108.

Wilbertz JH, Voigt F, Horvathova I, Roth G, Zhan Y, Chao JA. Single-Molecule Imaging of mRNA Localization and Regulation during the Integrated Stress Response. Molecular Cell. 2019 Mar; 73(5):946–958.e7. https://linkinghub.elsevier.com/retrieve/pii/S1097276518310360, doi: 10.1016/j.molcel.2018.12.006.

Wildner C, Mehta GD, Ball DA, Karpova TS, Koeppl H. Bayesian analysis dissects kinetic modulation during non-stationary gene expression. bioRxiv. 2023; doi: https://doi.org/10.1101/2023.06.20.545522.

Wills AG, Schön TB. Sequential Monte Carlo: A Unified Review. Annual Review of Control, Robotics, and Autonomous Systems. 2023 May; 6(1):159–182. http://dx.doi.org/10.1146/annurev-control-042920-015119, doi: 10.1146/annurev-control-042920-015119.

Wu CCC, Peterson A, Zinshteyn B, Regot S, Green R. Ribosome Collisions Trigger General Stress Responses to Regulate Cell Fate. Cell. 2020 Jun; 0(0). https://www.cell.com/cell/abstract/S0092-8674(20)30693-0, doi: 10.1016/j.cell.2020.06.006, publisher: Elsevier.

Wu Q, Medina SG, Kushawah G, DeVore ML, Castellano LA, Hand JM, Wright M, Bazzini AA. Translation affects mRNA stability in a codon-dependent manner in human cells. eLife. 2019 Apr; 8:e45396. https://elifesciences.org/articles/45396, doi: 10.7554/eLife.45396.

Yan X, Hoek TA, Vale RD, Tanenbaum ME. Dynamics of Translation of Single mRNA Molecules In Vivo. Cell. 2016 May; 165(4):976–989. https://linkinghub.elsevier.com/retrieve/pii/S0092867416304779, doi: 10.1016/j.cell.2016.04.034.

Zia RKP, Dong JJ, Schmittmann B. Modeling Translation in Protein Synthesis with TASEP: A Tutorial and Recent Developments. Journal of Statistical Physics. 2011 Aug; 144(2):405–428. http://arxiv.org/abs/1108.3312http://dx.doi.org/10.1007/s10955-011-0183-1, doi: 10.1007/s10955-011-0183-1, _eprint: 1108.3312.

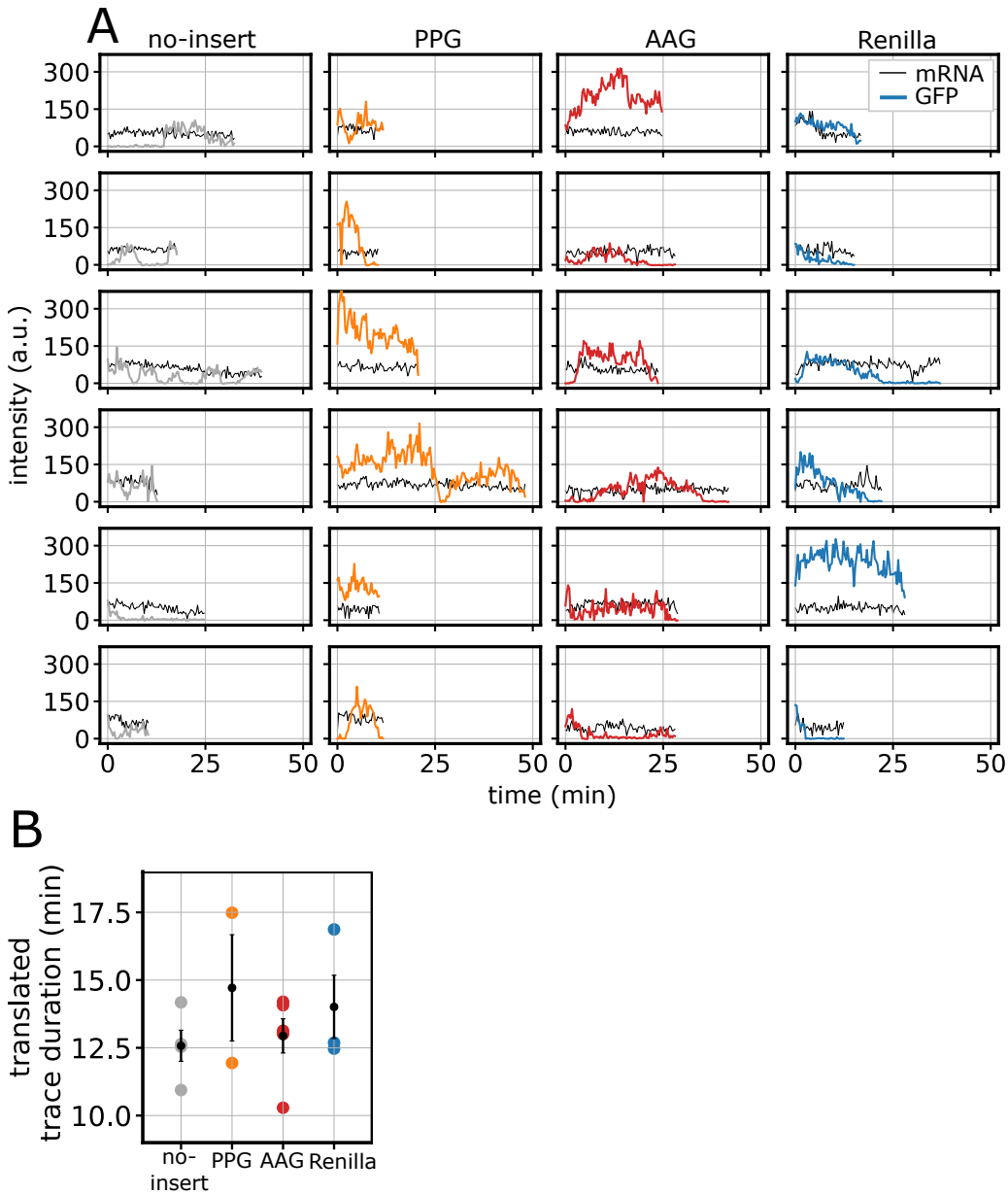

Figure 1—figure supplement 1. SunTag traces in control conditions. (A) Representative SunTag traces for different reporters in control conditions. **(B)** Duration of translated traces in control conditions (in black, average between experiments ± SEM).

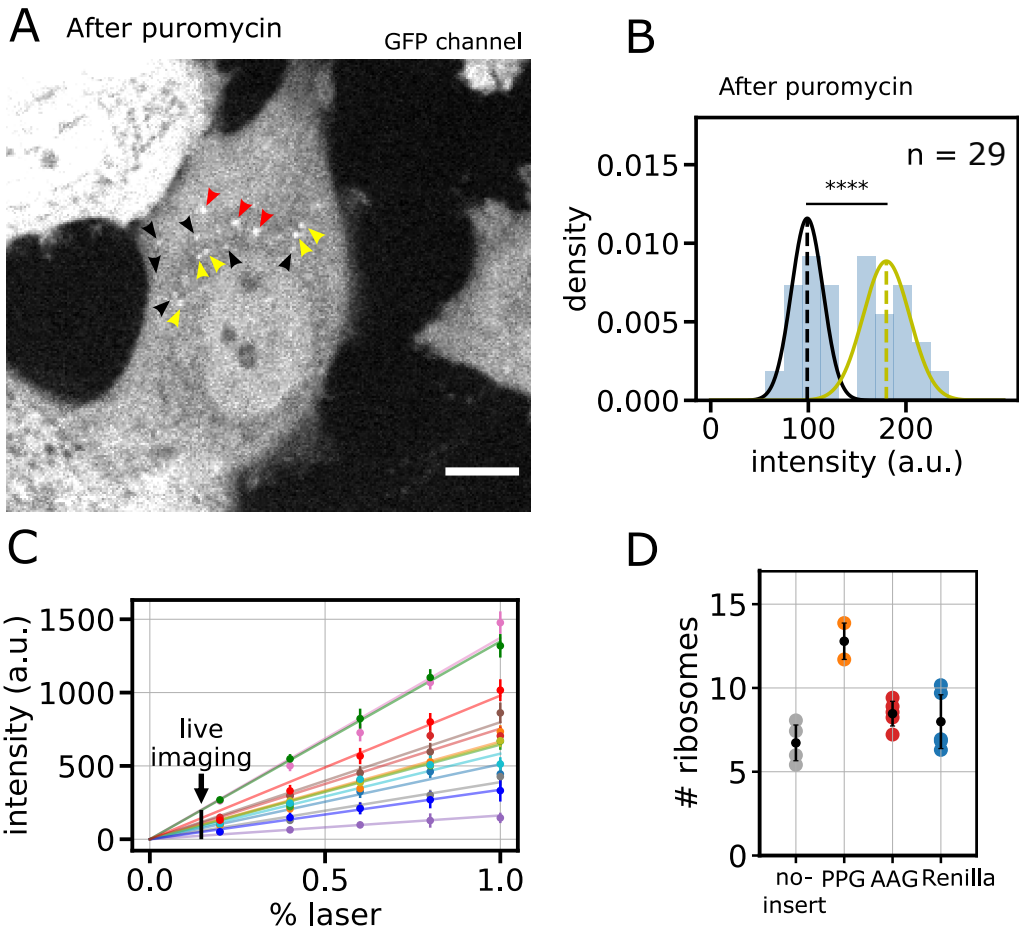

Figure 1—figure supplement 2. Experimental measurement of mature protein intensities to estimate number of translating ribosomes. A) Diffraction-limited spots in puromycin-treated cell expressing SunTag-Renilla-RH1-MS2, GFP channel. SunTag mature proteins are tethered to actin via the RH1 domain, that prevents their free diffusion in the cytoplasm, allowing to measure their intensity. Because of the low intensity, cells were imaged at 100% laser power. Black, yellow and red arrows indicate spots of different sizes and intensities. The image is part of a larger field-of-view, acquired with a 60X oil-objective. Scale bar: 10 μm. **B)** Histogram showing the average intensity distribution of 29 spots of lower intensity, after puromycin treatment, at 100% laser power. Black and yellow lines represent gaussian fits of a lower intensity (black) and a higher intensity (yellow) spot population. **C)** GFP intensity at increasing laser power of CHX-treated SunTag reporters. After CHX treatment, the intensity of the GFP signal is constant because translating ribosomes are blocked on the mRNA. This allows to estimate the dependence of measured intensity on laser power, which results to be linear. Each color represents one CHX-treated mRNA imaged at increasing laser power. **(D)** Number of ribosomes per translated period in traces longer than 20 min (in black, average across experiments ± SEM), as determined from the measurement of one mature protein intensity (A–C).

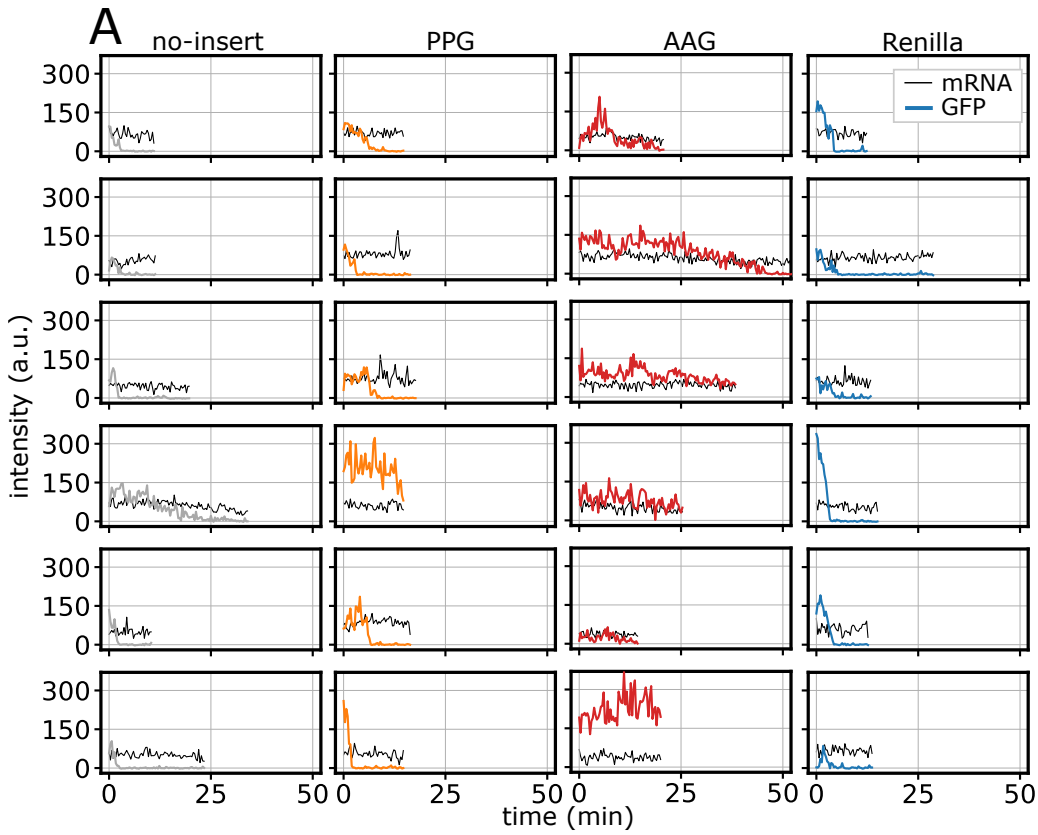

Figure 2—figure supplement 1. SunTag run-off traces in control conditions after HT addition.
(A) Representative SunTag traces for different reporters in control conditions after HT addition.

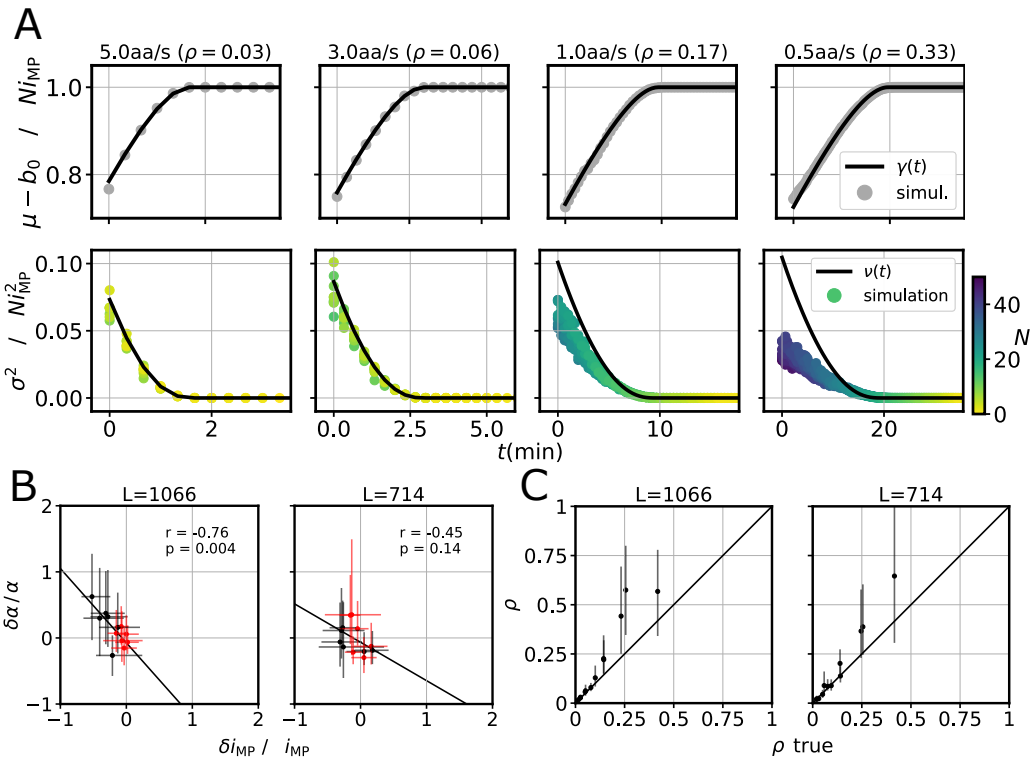

Figure 2—figure supplement 2. TASEP-based inference accurately estimates ribosome density on simulated data despite correlations between α and i_{MP}. A) Agreement of $\gamma(t)$ (top) and $\nu(t)$ (bottom) with simulations for different values of λ, with $\alpha = 1/30\mathrm{s}^{-1}$. While λ decreases (left to right) the average ribosome density ρ increases and the agreement between $\nu(t)$ and simulations significantly deteriorates. **B)** Correlation between the relative error on α and the relative error on i_{MP}, for $L = 1066$aa and $L = 714$aa and $s_0 = 0.4$. Black and red dots represents data with $\rho > 0.10$ and $\rho \leq 0.10$, respectively. The Pearson correlation coefficient r and the p-value p is indicated for all data ($n = 12$ simulations) and the black line shows the linear fit. The initiation rate α and on the mature protein intensity i_{MP} are negatively correlated, but at low densities ($\rho < 0.10$) the mature protein intensity is inferred more accurately and the correlation is less important. Simulation parameters: $\lambda \in \{0.5, 1, 3, 5\}$ aa/s, $\alpha \in \{1/120, 1/60, 1/30\}$ s^{-1}, $i_{\mathrm{MP}} = 10$ a.u. **C)** Inferred average density $\rho = \alpha\ell/\lambda$ at the beginning of run-off *vs* true average density as measured in simulations ($s_0 = 0.4$). The black line shows the $y = x$ line. In all panels error bars represent 95%-confidence intervals.

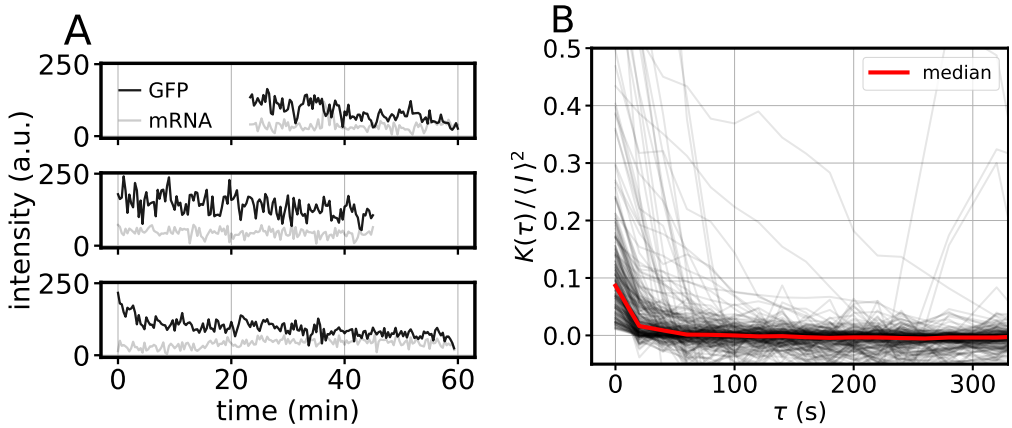

Figure 3—figure supplement 1. Global measurement noise estimation from CHX traces. A) Examples of GFP intensity traces after CHX treatment (black) and corresponding mRNA signal (grey). **B)** Autocorrelation $K(\tau)$ normalized by the square of the temporal mean intensity $\langle I \rangle^2$ for each CHX-treated trace (black lines) and median over all traces (red line), for different time delays τ. $K(0)/\langle I \rangle^2$ averaged over 236 traces yields an estimate of the multiplicative noise factor.

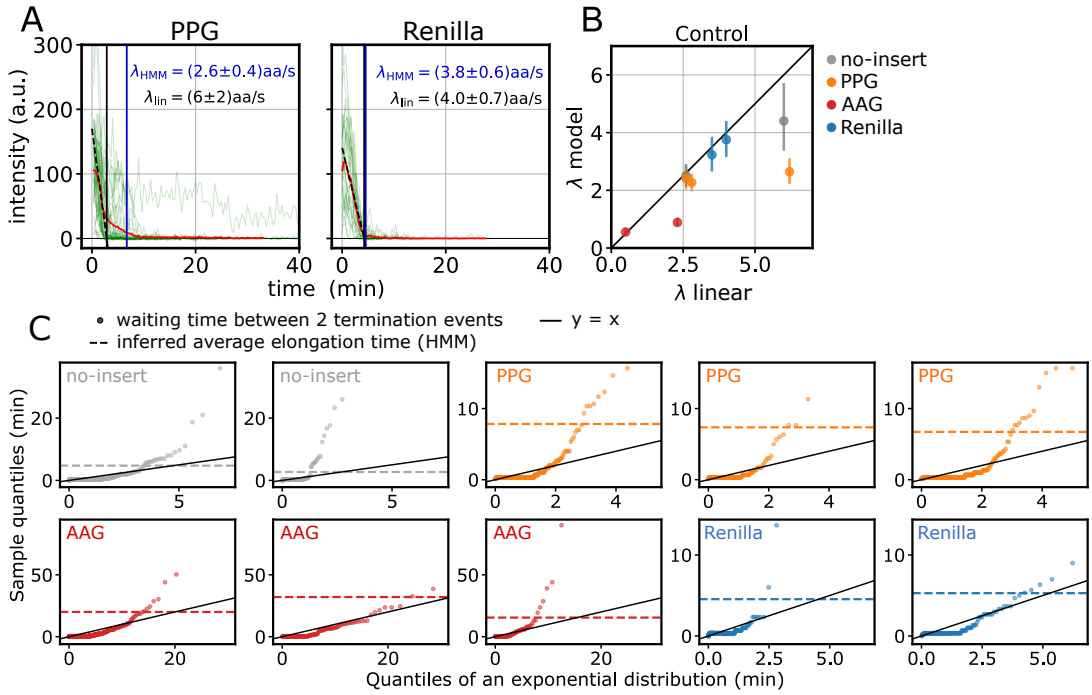

Figure 3—figure supplement 2. HMM approach predicts lower elongation speed than simple linear regression and suggests the presence of bursting and stalling. (A) Harringtonine run-off traces of PPG and Renilla (2 acquisitions). The black dashed line represents a linear regression of the average intensity decay (red). Vertical lines indicates the total elongation time as predicted by the linear fit (black) or by the HMM (blue). **(B)** Elongation rate predicted by the HMM *vs* elongation rate predicted by the linear-regression approach. **(C)** Q-Q plot of the waiting times between termination events, compared to an exponential distribution with mean the inverse initiation rate (as inferred by the HMM). Each plot represents one acquisition, and each dot the time between two termination events. The dashed line represents the total elongation time as inferred by the HMM model, and the full line the bisector. Waiting times lying above the dashed line are likely to be strong stalling events.

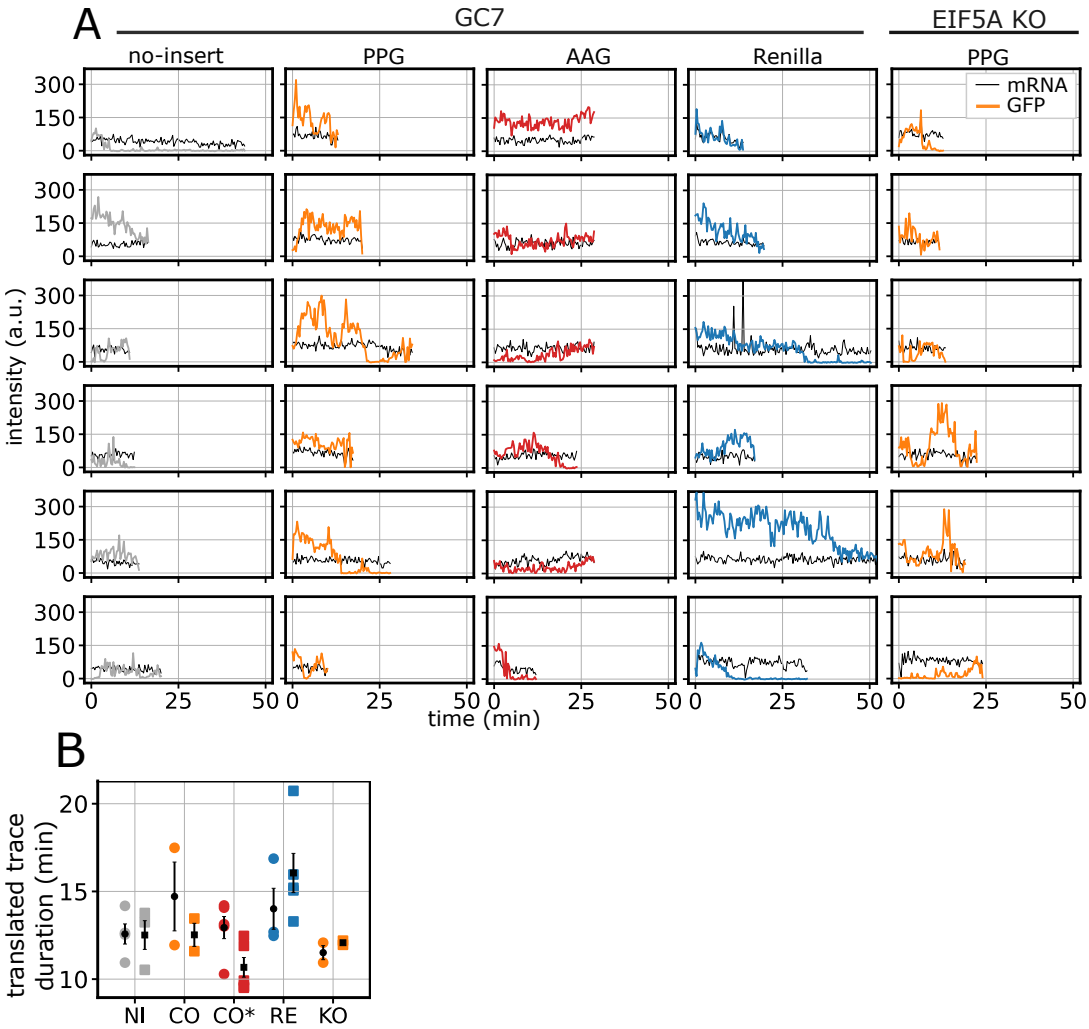

Figure 4—figure supplement 1. SunTag traces in perturbed conditions. (A) Representative SunTag traces for different reporters in perturbed (GC7/EIF5A KO) conditions. **(B)** Duration of translated traces in perturbed conditions (average across experiments ± SEM).

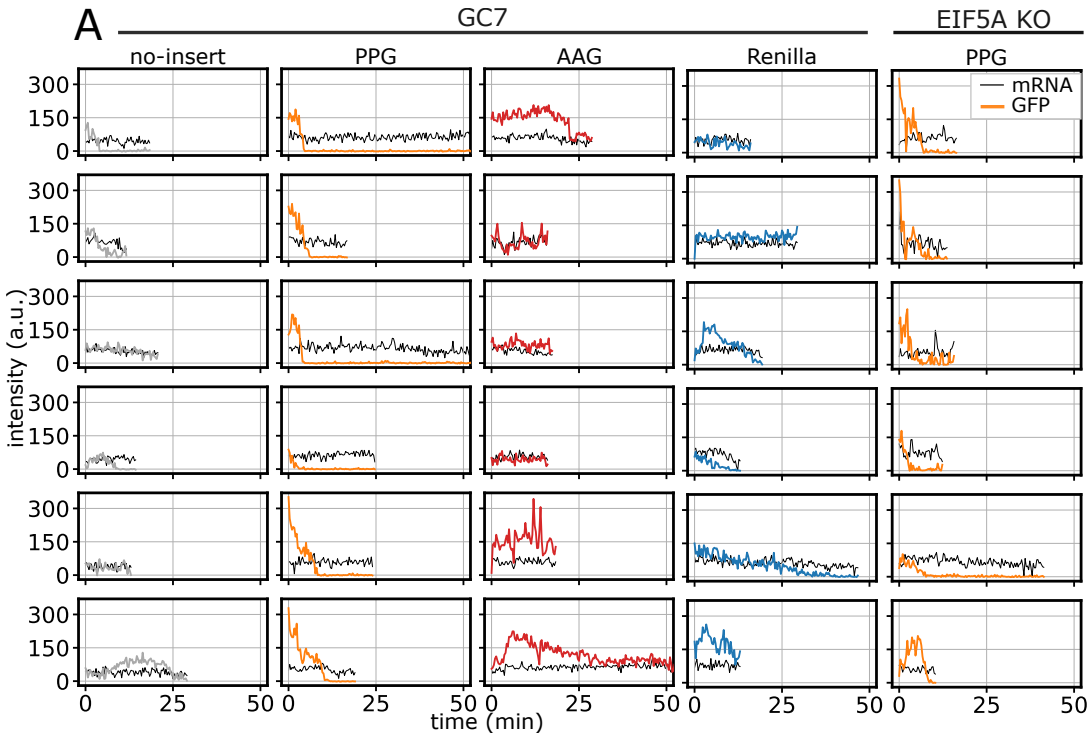

Figure 5—figure supplement 1. SunTag run-off traces in perturbed conditions after HT addition. (A) Representative SunTag traces for different reporters in perturbed conditions (GC7/EIF5A KO) after HT addition.

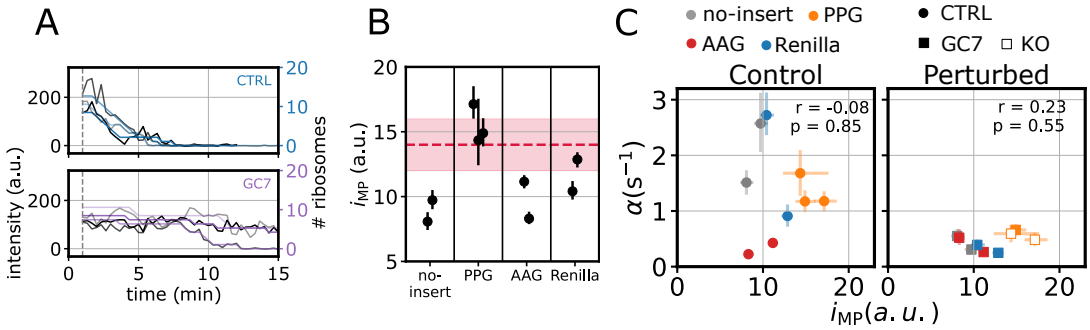

Figure 5—figure supplement 2. Inferred mature protein intensities are in good agreement with the experimental measurement. A) Representative PPG traces in control and GC7-treated conditions, together with the inferred number of ribosomes. **B)** Mature protein intensity i_{MP} for each experiment, subdivided by reporter. The red dashed line indicates the mature protein intensity as measured by an independent calibration experiment and the filled area the uncertainty on the measurement. **C)** Initiation rate *vs* mature protein intensity, for both control and perturbed conditions ($n = 10$ experiments): α initiation rate and i_{MP} mature protein intensity.